

Anisotropic Gauss Reconstruction for Unoriented Point Clouds

ANONYMOUS AUTHOR(S)

Unoriented surface reconstructions based on the Gauss formula have attracted much attention due to their elegant mathematical formulation and excellent performance. However, the isotropic characteristics of the formulation limit their capacity to leverage the anisotropic information within the point cloud. In this work, we propose a novel anisotropic formulation by introducing a convection term in the original Laplace operator. By choosing different velocity vectors, the anisotropic feature can be exploited to construct more effective linear equations. Moreover, an adaptive selection strategy is introduced for the velocity vector to further enhance the orientation and reconstruction performance of thin structures. Extensive experiments demonstrate that our method achieves state-of-the-art performance and manages various challenging situations, especially for models with thin structures or small holes. The source code will be released on GitHub.

Additional Key Words and Phrases: Geometric modeling, Surface reconstruction, Orientation, Gauss formula

1 INTRODUCTION

Due to the convenience of point cloud acquisition, surface reconstruction plays a crucial role in computer graphics with a wide range of applications, such as geographic information systems, medical image processing, environmental modeling, and building visualization.

In the past few decades, several well-established surface reconstruction methods have been proposed with remarkable performance. Kazhdan et al. [2006]; Kazhdan and Hoppe [2013] proposed converting the reconstruction problem into a spatial Poisson problem with additional constraints. Manson et al. [2008] chose orthogonal wavelet bases to calculate the indicator field. Lu et al. [2019] introduce the Gauss formula to surface reconstruction and apply a modified kernel to address the near-singularity problem in computation. However, these methods have limitations in the requirement of oriented normals. In recent years, some attempts have been made for unoriented surface reconstruction. VIPSS [Huang et al. 2019] minimizes Duchon’s energy using L-BFGS. Iterative Poisson surface reconstruction (iPSR) [Hou et al. 2022] introduces the idea of normal iteration. Parametric Gauss reconstruction (PGR) [Lin et al. 2023] constructs the linear system from the isotropic Gauss formula to calculate the linearized surface element. Converting unoriented point clouds into the oriented representation provides a novel approach to surface reconstruction. Xu et al. [2023a] proposed a smooth nonlinear objective function to characterize the requirements of an acceptable winding-number field, turn the problem into an unconstrained optimization problem, and reconstruct the surface by SPR.

Although there are many mature studies, surface reconstruction for unoriented points is still a challenging task. We notice that PGR gives us a good idea of reconstructing the surface by calculating the indicator function. However, PGR needs to solve under-determined equation systems and is sensitive to the regularization of equations. There is still room for improvement. This paper showcases our new research effort towards handling unoriented point clouds for both orientation and reconstruction. Considering that the isotropic Gauss formula will lead to the problem of lack of equations, we

propose introducing a convection term in the original Laplace operator to obtain the anisotropic fundamental solution. Using the divergence theorem and double-layer potential theory, we derive the corresponding anisotropic Gauss formula to produce the indicator field. By choosing different velocity vectors as convection terms, the anisotropic Gauss formula constructs more linear equations to eliminate the dilemma of lack of equations. In addition, we provide two methods for solving under-determined and over-determined equations, respectively, and propose the blocking matrix strategy to save memory. Due to the introduction of anisotropy, our method reduces the sensitivity to the regularization of the equations. Our method can output the points’ unit outward normals by normalizing the solution of the equations and can extract surfaces by the value of the indicator function on the query points with marching cubes.

Moreover, the quality of velocity vectors can affect the performance of orientation and reconstruction. Therefore, we propose a novel adaptive selection strategy, especially for dealing with thin structures by principal component analysis (PCA) and singular value decomposition (SVD). We put forward detailed ideas for improving our method. We conduct thorough comparisons with other well-known methods through comprehensive experiments, which showcase our method’s effectiveness and scalability on famous datasets, including thin structures, outliers, and noisy or sparse point clouds.

Our main contributions can be summarized as follows.

- We introduce a convection term in the original Laplace operator to extend the Gauss formula into an anisotropic form.
- By introducing the anisotropy, we construct more linear equations and decrease the sensitivity to regularization.
- We propose a novel adaptive selection strategy for velocity vectors, which can further improve orientation and reconstruction results, especially for point clouds with thin structures or small holes.

2 RELATED WORK

2.1 Surface Reconstruction based on Implicit Function

The goal of implicit-based methods is to construct an implicit function or implicit field and make the input point cloud lie on one of its level sets. The task of surface reconstruction has been extensively researched in the past decades, and we classify these methods into two categories based on whether the normal information of the point cloud is needed.

2.1.1 Surface Reconstruction for Oriented Point Clouds. The radial basis function methods treat each point in the point cloud as the center of a radial basis function and adjust the weights of these functions to approximate the signed distance function (SDF). To solve larger scale point clouds problem, Morse et al. [2001], Walder et al. [2006] proposed to use compactly supported radial bases. In order to further improve the results and utilize normal information, Macêdo et al. [2011], Ijiri et al. [2013], Liu et al. [2016] propose to use Hermite RBFs to interpolate points’ positions and normals together. Implicit moving least squares (IMLS) fit local algebraic

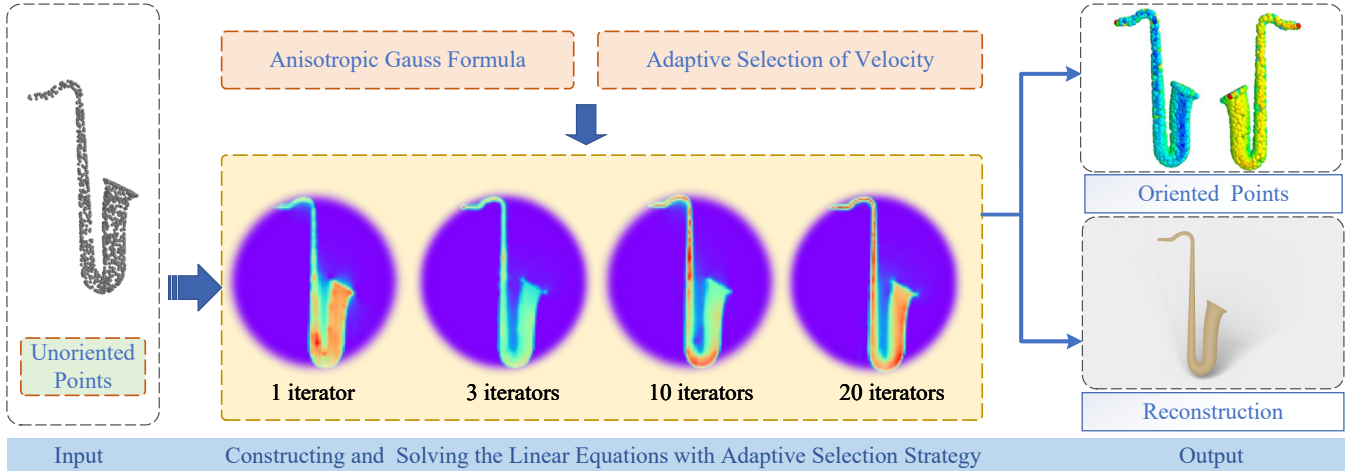


Fig. 1. We propose a novel anisotropic formulation by introducing a convection term in the original Laplace equation. By choosing different velocity vectors, we can fully take advantage of the anisotropic feature. Our method establishes and solves equation systems by the inputting unoriented points, simultaneously accomplishing orientation and reconstruction tasks. The color of the output point cloud in the top right-hand corner of the figure represents the normal information. Extensive experiments demonstrate that our method achieves state-of-the-art performance in both orientation and surface reconstruction for unoriented point clouds.

shapes and minimize the total squared errors to nearby points and normals, such as [Dey and Sun 2005], [Kolluri 2008].

In addition to approximation and fitting, Stokes’ theorem provides new inspiration. [Kazhdan 2005], [Manson et al. 2008], [Ren et al. 2018], and [Lu et al. 2019] respectively choose Fourier bases, orthogonal wavelet bases, biorthogonal wavelet bases, isotropic fundamental solution of Laplace function, and compute the corresponding coefficient. [Kazhdan 2005] has a breakneck running speed at that time by using fast Fourier transforms (FFT). Manson et al. [2008] utilizes the orthogonal compact support property of wavelet basis functions to maintain linear computational complexity and handle multi-scale reconstruction. This algorithm not only runs fast but also has the potential to handle large-scale point clouds. Ren et al. [2018] further expands the selection space of wavelet bases. Lu et al. [2019] introduces the Gauss formula to surface reconstruction problems and has good reconstruction results.

Another popular choice is converting the reconstruction problem into a spatial Poisson problem, which has achieved good reconstruction results. This novel idea is first proposed in [Kazhdan et al. 2006]. [Calakli and Taubin 2011; Kazhdan et al. 2020; Kazhdan and Hoppe 2013] fit the smoothed indicator function near the target surface and enhance algorithm performance by adding different constraint information.

2.1.2 Surface Reconstruction for Unoriented Point Clouds. Attributed to the inherent challenge of acquiring normal information, numerous point clouds, particularly those derived from real-world data, encounter difficulties in being properly oriented. While addressing this issue is more complex and challenging, it has significant practical implications and potential applications. Much attention has been paid to such a problem.

Deep learning methods have been gradually introduced and thoroughly studied in surface reconstruction in recent years. These

methods represent implicit fields with neural networks. Point2surf (P2S) [Erler et al. 2020] improves generalization performance and reconstruction accuracy by learning a prior over a combination of detailed local patches and coarse global information. [Gropp et al. 2020] (IGR) proposes a new paradigm for computing high-fidelity implicit neural representations based on implicit geometric regularization. DiGS [Ben-Shabat et al. 2022] incorporates soft second-order derivative constraints to guide the INR learning process, leading to better representations. Neural-Singular-Hessian (NSH) [Wang et al. 2023] enforces the Hessian of the neural implicit function to have a zero determinant for points near the surface, which suppresses ghost geometry and recovers details from unoriented point clouds with better expressiveness. However, these deep learning methods often require long-term training and solving time. Moreover, due to memory limitations, these methods often only handle sparse point clouds with weak robustness.

In recent years, some research has been proposed on handling unoriented point clouds based on traditional methods. These methods are primarily based on the mature oriented surface reconstruction methods with clever designs to eliminate the dependence on normals. Shape as points (SAP) [Peng et al. 2021] revisits the classic point cloud representation and introduces a differentiable point-to-mesh layer by using a differentiable formulation of PSR [Kazhdan et al. 2006]. Also based on PSR [Kazhdan et al. 2006], iterative Poisson surface reconstruction (iPSR) [Hou et al. 2022] computes the normals from the surface in the preceding iteration and then generates a new surface with better quality. Based on GR [Lu et al. 2019], parametric Gauss reconstruction (PGR) [Lin et al. 2023] takes unoriented point clouds as input and solves for a set of linearized surface elements that produce the indicator field represented by the Gauss formula.

2.2 Normal Consistent Orientations for Point Clouds

Calculating high-quality normals for unoriented point clouds is an important topic in geometric modeling and computer graphics. Converting unoriented point clouds into the oriented representation provides a novel approach to surface reconstruction. Overall, we can divide them into optimization-based and learning-based methods.

Optimization-based Methods The research on optimization-based methods has a long history, which can date back to the last century. The pioneering work uses principal component analysis (PCA) to initialize normal orientations by Hoppe et al. [1992]. Although many propagation-based methods have emerged, these methods always fail to handle complex or separated point clouds.

Over the years, many technologies have been proposed to mitigate the problems of relying solely on local information. Dipole [Metzger et al. 2021] uses dipole propagation across patches iteratively. VIPSS [Huang et al. 2019] minimizes the Duchon’s energy with the L-BFGS algorithm. Xu et al. [2023b] propose a smooth nonlinear objective function to characterize the requirements of an acceptable winding-number field [McIntyre and Cairns 1993] and turn the problem into an unconstrained optimization problem. Xiao et al. [2023] propose combined iso-value constraints with local consistency requirements for normals to construct optimization formulation.

Learning-based Methods Learning-based methods often treat oriented normal estimation as a classification or regression task where the normals are directly regressed from the feature extracted from the local patches. PCPNet [Guerrero et al. 2018] encodes the multiple-scale features of local patches in a structured manner, which enables one to estimate local shape properties such as normals and curvature. Li et al. [2023] propose a method for oriented normal estimation by aggregating the local and global information and learning signed hypersurfaces end-to-end.

Due to the tight link between orientation and surface reconstruction, some proposed state-of-the-art methods can simultaneously accomplish orientation and surface reconstruction tasks. For example, as reconstruction methods, iPSR [Hou et al. 2022] and PGR [Lin et al. 2023] both have the potential for orientation. The former can output the estimated normals from the estimated surface, while the latter can obtain the normals from the solution of the equation. However, iPSR [Hou et al. 2022] cannot be regarded as an orientation method strictly due to its resample of the input point cloud, especially for dense or noisy point clouds. Due to the lack of equations in PGR [Lin et al. 2023], there is room for further improvement in the orientation accuracy. This is also one of the motivations of our method.

3 MOTIVATION

An important and popular way to reconstruct the surfaces from the unoriented point clouds is to calculate the indicator function χ . The Gauss formula provides a novel and powerful tool to represent the indicator function as a boundary integral.

In detail, let $\Omega \subset \mathbb{R}^3$ be an open and bounded region with the smooth boundary $\partial\Omega$. The indicator function $\chi(\mathbf{x})$ of Ω can be



Fig. 2. By introducing anisotropy, our method not only improves the quality of surface reconstruction but also stimulates the potential of the Gauss formula for orientation.

calculated through divergence theorem

$$\int_{\partial\Omega} \frac{\partial\Phi(\mathbf{x} - \mathbf{y})}{\partial\mathbf{n}(\mathbf{y})} dS(\mathbf{y}) = \chi(\mathbf{x}) = \begin{cases} 0 & \mathbf{x} \in \mathbb{R}^3 \setminus \bar{\Omega} \\ \frac{1}{2} & \mathbf{x} \in \partial\Omega \\ 1 & \mathbf{x} \in \Omega, \end{cases}$$

where

$$\Phi(\mathbf{x}) = \frac{1}{4\pi|\mathbf{x}|}$$

is the three-dimensional fundamental solution, which can be obtained by using symmetry to find its radial solution in Appendix A. $\bar{\Omega}$ represents the closure of the region Ω , $\mathbf{n}(\mathbf{y})$ represents the outward unit normal vector at any point $\mathbf{y} \in \partial\Omega$ and $dS(\mathbf{y})$ denotes the surface element of the point \mathbf{y} . $|\cdot|$ represents the L_2 norm of vectors. The proof will be presented as a special case of our generalized theorem later. The n -dimensional Gauss formula can be obtained by replacing $\Phi(\mathbf{x})$ with the n -dimensional Laplace fundamental solution in equation (21).

As shown in GR[Lu et al. 2019] and PGR[Lin et al. 2023], reconstructing the surfaces through the Gauss formula is feasible with good reconstruction results. However, PGR needs to solve under-determined equation systems. For $\mathcal{P} = \{\mathbf{p}_i\}_{i=1}^N$, the isotropic Gauss formula can only construct N non-homogeneous equations, but there are $3N$ unknown variables. In addition, PGR is sensitive to the regularization of equations and shows poor performance under the inappropriate regularization value, which is shown in the supplementary material.

Extensive experiments show that PGR still has room for improvement in orientation, normal estimation, and surface reconstruction. On the one hand, the normals estimated by PGR deviate greatly from the ground truth. On the other hand, due to its reliance on isotropic fundamental solutions, PGR suffers from poor reconstructions for point clouds with thin structures or small holes.

The isotropic Gauss formula utilizes the information of point clouds incompletely. It does not incorporate the geometric characteristics of the point cloud, especially the direction information. Due to the lack of equations and information, it is difficult to completely avoid the singularity of linear equations, leading to a strong dependence on regularization.

Inspired by this observation, we propose to stimulate the potential of the Gauss formula for reconstruction and orientation by introducing the anisotropy and constructing more equations to make full use of point cloud information. To generalize the fundamental solution, we add convection terms, including velocity vectors and first-order derivatives, into the original Laplace equation,

$$\Delta u - \mathbf{c} \cdot \nabla u = 0, \quad (1)$$

where $\mathbf{c} \in \mathbb{R}^3$.

We refer to the solution of equation (3) as the anisotropic fundamental solution, denoted as $\Phi_{\mathbf{c}}$. We can derive an analytical solution

$$\Phi_{\mathbf{c}}(\mathbf{x}) = \frac{1}{4\pi|\mathbf{x}|} e^{\frac{1}{2}(\mathbf{c} \cdot \mathbf{x} - |\mathbf{c}||\mathbf{x}|)}, \quad (2)$$

with the gradient of it,

$$\nabla \Phi_{\mathbf{c}}(\mathbf{x}) = \frac{1}{4\pi|\mathbf{x}|} e^{\frac{1}{2}(\mathbf{c} \cdot \mathbf{x} - |\mathbf{c}||\mathbf{x}|)} \left(-\frac{\mathbf{x}}{|\mathbf{x}|^2} + \frac{1}{2}\mathbf{c} - \frac{1}{2}|\mathbf{c}| \frac{\mathbf{x}}{|\mathbf{x}|} \right). \quad (3)$$

When $\mathbf{c} = (0, 0, 0)^T$, the anisotropic fundamental solution degenerates to be the isotropic solution Φ . $|\cdot|$ represents the L_2 norm of vectors. **The complete and detailed theoretical derivation of the theorem is provided in Appendix B.**

Using the divergence theorem and double layer potential theory, we can derive the anisotropic Gauss formula corresponding to (2).

THEOREM 1 (ANISOTROPIC GAUSS FORMULA). *Let $\Omega \subset \mathbb{R}^3$ be an open and bounded region with the smooth boundary $\partial\Omega$, then the indicator function $\chi(\mathbf{x})$ of the region Ω can be calculated through the anisotropic fundamental solution (2). In detail,*

$$\chi(\mathbf{x}) = \int_{\partial\Omega} K_{\mathbf{c}}(\mathbf{x} - \mathbf{y}) \cdot \mathbf{n}(\mathbf{y}) dS(\mathbf{y}), \quad (4)$$

where

$$K_{\mathbf{c}}(\mathbf{x}) = \nabla \Phi_{\mathbf{c}} - \mathbf{c} \cdot \Phi_{\mathbf{c}} = \frac{1}{4\pi|\mathbf{x}|} e^{\frac{1}{2}(\mathbf{c} \cdot \mathbf{x} - |\mathbf{c}||\mathbf{x}|)} \left(-\frac{\mathbf{x}}{|\mathbf{x}|^2} - \frac{1}{2}\mathbf{c} - \frac{1}{2}|\mathbf{c}| \frac{\mathbf{x}}{|\mathbf{x}|} \right), \quad (5)$$

and $\mathbf{N}(\mathbf{y})$ represents the outward unit normal vector at any point $\mathbf{y} \in \partial\Omega$ and $dS(\mathbf{y})$ denotes the surface element of the point \mathbf{y} . $|\cdot|$ represents the L_2 norm of vectors.

The complete and detailed theoretical derivation of the Theorem 1 is provided in Appendix C. When $\mathbf{c} = (0, 0, 0)^T$, the anisotropic Gauss formula degenerates to be the isotropic Gauss formula.

4 METHOD

Let the target area $\Omega \subset \mathbb{R}^3$ be an open and bounded region with the smooth boundary $\partial\Omega$. The input point cloud is the points on the surface, $\mathcal{P} \in \partial\Omega$.

4.1 Discretizing the Anisotropic Gauss Formula

We first discretize the integral in equation (4).

$$\begin{aligned} \chi(\mathbf{x}) &= \int_{\partial\Omega} K_{\mathbf{c}}(\mathbf{x} - \mathbf{y}) \cdot \mathbf{n}(\mathbf{y}) dS(\mathbf{y}) \\ &\approx \sum_{j=1}^N \varphi_j^{\mathbf{c}}(\mathbf{x}) \cdot \mathbf{n}_{\mathbf{p}_j} \sigma_{\mathbf{p}_j}, \end{aligned} \quad (6)$$

where

$$\varphi_j^{\mathbf{c}}(\mathbf{x}) = \frac{1}{8\pi|\mathbf{x} - \mathbf{p}_j|} e^{\frac{1}{2}(\mathbf{c} \cdot (\mathbf{x} - \mathbf{p}_j) - |\mathbf{c}||\mathbf{x} - \mathbf{p}_j|)} \left(-\frac{2(\mathbf{x} - \mathbf{p}_j)}{|\mathbf{x} - \mathbf{p}_j|^2} - \mathbf{c} - |\mathbf{c}| \frac{\mathbf{x} - \mathbf{p}_j}{|\mathbf{x} - \mathbf{p}_j|} \right),$$

$\mathbf{n}_{\mathbf{p}_j}$ represents the outward unit normal vector at the point \mathbf{p}_j , and $\sigma_{\mathbf{p}_j}$ denotes the surface element of the point \mathbf{p}_j . $|\cdot|$ represents the L_2 norm of vectors. Since we know the location information of the point cloud, $\varphi_j^{\mathbf{c}}(\mathbf{x}) = (\varphi_{j,1}^{\mathbf{c}}(\mathbf{x}), \varphi_{j,2}^{\mathbf{c}}(\mathbf{x}), \varphi_{j,3}^{\mathbf{c}}(\mathbf{x}))$ in the equation (6) are known variables, while the only unknown variables are the normal and area elements.

We denote the 3-dimensional vector

$$\mu_j = (\mu_{j,1}, \mu_{j,2}, \mu_{j,3}) \triangleq \mathbf{n}_{\mathbf{p}_j} \sigma_{\mathbf{p}_j} \quad (7)$$

to estimate area and normal information of \mathbf{p}_j and be called as **linearized surface element (LSE)**. Then, the anisotropic Gauss formula has a discrete form

$$\chi(\mathbf{x}) \approx \sum_{j=1}^N \sum_{k=1}^3 \varphi_{j,k}^{\mathbf{c}}(\mathbf{x}) \mu_{j,k} \quad (8)$$

that can be used to calculate the indicator function of Ω . Although, due to the lack of the outward normals, we cannot calculate the indicator function by estimating $\mu_{j,k}$ directly. However, we can still utilize the fact that the value of the indicator function at any point on the surface is $\frac{1}{2}$ to construct the equation systems. Then, we solve the equations to obtain the value of $\mu_{j,k}$.

4.2 Constructing and Solving the Linear Equations

For any fixed velocity vector \mathbf{c} , we select the input points \mathbf{p}_i , $i = 1, 2, 3, \dots, N$ as the query point \mathbf{x} in equation (8) sequentially, which lie on the surface of the region. Then, according to Theorem 1,

$$\sum_{j=1}^N \sum_{k=1}^3 \varphi_{j,k}^{\mathbf{c}}(\mathbf{p}_i) \mu_{j,k} = \frac{1}{2}, \quad i = 1, 2, 3, \dots, N,$$

and we denote it as

$$A_i^{\mathbf{c}}(\mathbf{p}_i; \mathcal{P}) \mu = \frac{1}{2}, \quad i = 1, 2, 3, \dots, N \quad (9)$$

for brevity, where $\mu \in \mathbb{R}^{3N \times 1}$ denotes the flattened vector of $\mu_{j,k}$, and $A_i^{\mathbf{c}} \in \mathbb{R}^{1 \times 3N}$ is a row vector to represent the flattened vector of $\varphi_{j,k}^{\mathbf{c}}(\mathbf{p}_i)$. It should be pointed out that the selection of query points and velocity vectors is independent. We can choose different velocity vectors $\mathbf{c}_{\mathbf{p}_i,s}$ for different point \mathbf{p}_i based on the characteristics of such point, and there is no limit to the number s of velocity vectors.

In order to reduce the number of hyperparameters, we select a fixed velocity vector \mathbf{c} to generate N equations. Namely

$$A^{\mathbf{c}}(\mathcal{P}; \mathcal{P}) \mu = \frac{1}{2}. \quad (10)$$

However, when $\mathbf{x} = \mathbf{y} = \mathbf{p}_j$, the equation is singular and cannot be ignored. The singularity may lead to an increase in error and a decrease in stability, orientation, and reconstruction. Hence, we modify the distance function $d(\mathbf{x}, \mathbf{p}_j) = |\mathbf{x} - \mathbf{p}_j|$ as

$$\tilde{d}(\mathbf{x}, \mathbf{p}_j) = \max\{d(\mathbf{x}, \mathbf{p}_j), w(\mathbf{x})\},$$

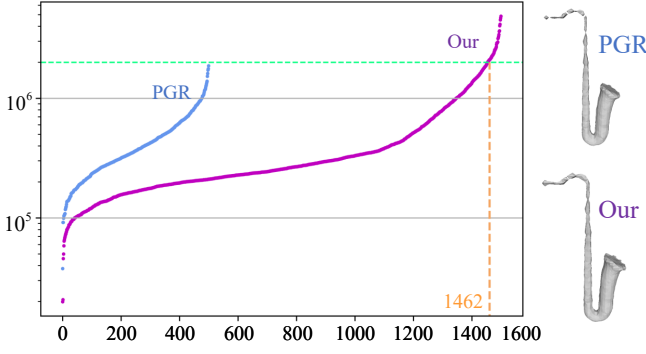


Fig. 3. Under the same input point cloud with 500 points and regularization value, our method reduces the singularity of matrix B and increases the number of effective equations compared to PGR.

where $w(\mathbf{x})$ is the width function to set the threshold of truncation. It is related to the average distance of the k closest points to the point cloud and can be calculated as

$$w(\mathbf{x}) = \max\{w_{\min}, \sqrt{\frac{1}{k_w} \sum_{\mathbf{p} \in \text{kNN}(\mathbf{x}; \mathcal{P})} |\mathbf{x} - \mathbf{p}|^2}\},$$

where $\text{kNN}(\mathbf{x}; \mathcal{P})$ represents the k nearest neighbors of \mathbf{x} in input point cloud \mathcal{P} , and w_{\min} , k_w are hyperparameters. In most examples, w_{\min} is suggested to be set as 0.0015. We denote the equation (10) after truncation as

$$A_{\mathbf{c}}(\mathcal{P}; \mathcal{P})\mu = \frac{1}{2}. \quad (11)$$

We have completed the construction of N equations induced by single velocity vector \mathbf{c} . However, as shown in the PGR, the information provided by a single velocity vector is insufficient. Therefore, choosing multiple velocity vectors to construct more equations is recommended.

For 3-dimensional point clouds \mathcal{P} with N points, the number of unknown variables is $3N$, but the number of equations varies with the selection of velocity vectors. Therefore, we provide two methods for solving under-determined and over-determined equations, respectively. When solving the square matrices, either approach can be used. We denote m as the number of selected velocity vectors.

4.2.1 Solving the Under-determined System. Storing and solving large-scale linear equation systems remains a challenging problem. The computational complexity can be no less than $O(N \log N)$ even with the fast multipole method (FMM) [Darve 2000]. Therefore, we tend to solve problems with as few equations as possible. Moreover, as the generalization of PGR, we tend to make our method fully backward compatible with it.

Then, we introduce the details of solving under-determined equation systems. Take the case of $m = 2$, when the coefficient matrix A is $2N \times 3N$ as example,

$$A\mu = \begin{bmatrix} A_{c_1}(\mathcal{P}; \mathcal{P}) \\ A_{c_2}(\mathcal{P}; \mathcal{P}) \end{bmatrix} \mu = d. \quad (12)$$

Therefore, the solution is not unique, and the natural idea is to find the solution with the minimum L_2 norm,

$$\min_{\mu} \|\mu\|_2, \quad \text{subject to } A\mu = d.$$

Similar to [Lin et al. 2023], it can be computed as

$$\mu = A^T \xi, \quad \text{with } B\xi = d, \quad (13)$$

where

$$B = B_0 + R_0, \\ B_0 = AA^T, \quad R_0 = (\alpha - 1) \cdot \text{diag}(B_0),$$

and R_0 acts as a regularization that can be any symmetric and positive-definite matrix. α is a hyperparameter. Thanks to the increase of anisotropy information in equations, our method can reduce the sensitivity to it, compared to PGR.

As the number of equations increases, calculating AA^T directly takes up too much memory. Therefore, we calculate the coefficient matrix B_0 by blocking matrix, which enables our method to handle point clouds with a larger scale. In detail, we set N_s as the batch size. Then $\mathcal{P} = \mathcal{P}_1 \cup \mathcal{P}_2 \cup \dots \cup \mathcal{P}_M$ with $P_i \cap P_j = \emptyset, \forall i \neq j$. For any i ,

$$A_{c_i}(\mathcal{P}; \mathcal{P}) = \begin{bmatrix} A_{c_i}(\mathcal{P}_1; \mathcal{P}) \\ \vdots \\ A_{c_i}(\mathcal{P}_M; \mathcal{P}) \end{bmatrix} \triangleq \begin{bmatrix} A_{c_i,1} \\ \vdots \\ A_{c_i,M} \end{bmatrix}, \quad (14)$$

where $M = \lceil \frac{N}{N_s} \rceil + 1$. For all $j \leq M$, the number of rows in $A_{c_i,j}$ is less than or equal to the hyperparameter N_s . Then, we use Einstein's summation and the symmetry of B_0 to calculate and assemble matrix B_0 in blocks.

$$(B_0)_{M*i_1+j_1, M*i_2+j_2} = A_{c_{i_1}, j_1} A_{c_{i_2}, j_2}^T, \quad (M*i_1 + j_1 \leq M*i_2 + j_2),$$

where $i_1, i_2 \leq m$, $j_1, j_2 \leq M$, and $(B_0)_{i,j}$ are the submatrixes with $(B_0)_{i,j} = (B_0)_{j,i}^T, \forall i > j$. In this way, we can make the memory required for calculating the coefficient matrix and B linear with the point cloud's size.

4.2.2 Solving the Over-determined System. Since the constructed equation system is nonlinear to the velocity vector \mathbf{c} , we can choose infinite velocity vectors with different directional information to construct the equations in theory. In order to fully utilize point cloud information and anisotropy, the idea of letting $m > 3$ is natural. At this point, the equations become an over-determined system. We take the case that the coefficient matrix A is $mN \times 3N$ as the example to describe the framework of solving the over-determined system.

At this point, the natural idea is to seek the least-squares solution

$$\min_{\mu} \|A\mu - d_m\|_2^2,$$

where $d_m = \frac{1}{2} \in \mathbb{R}^{mN \times 1}$, which has an equivalent form with

$$\min_{\mu} \sum_{i=1}^m \|A_{c_i} \mu - d_1\|_2^2, \quad (15)$$

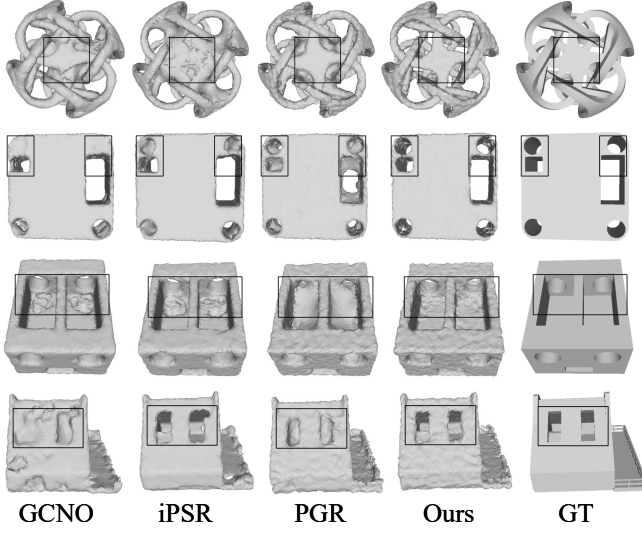


Fig. 4. The qualitative comparison of our method with PGR, iPSR, and GCNO+SPR on reconstruction. Our method can reconstruct surfaces with higher quality.

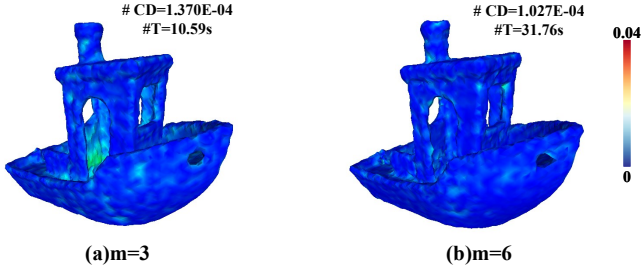


Fig. 5. The qualitative and quantitative comparison of equation quantity in our method. Choosing more velocity vectors can further slightly improve the performance.

where $d_1 = \frac{1}{2} \in \mathbb{R}^{N \times 1}$. Then, it can be computed as

$$H_0 \mu = \left(\sum_{i=1}^m A_{c_i}^T d_1 \right), \quad \text{with} \quad H_0 = \left(\sum_{i=1}^m A_{c_i}^T A_{c_i} \right).$$

However, H_0 is also difficult to avoid being ill-conditioned. For this, we put a similar nonuniform regularization

$$H \mu = \left(\sum_{i=1}^m A_{c_i}^T d_1 \right) \quad \text{with} \quad H = H_0 + \text{diag}(H_0), \quad (16)$$

Since B and H are symmetric matrices, we can use the *CG* algorithm to solve linear equations (13) and (16).

Although when $m = 3$, the coefficient matrix A still cannot be solved using the *CG* algorithm directly, either the *GMRES* algorithm or the methods mentioned above can be used to solve it.

The qualitative and quantitative results of choosing different numbers m of velocity vectors for reconstruction are compared in Figure 5. Choosing more velocity vectors can add more anisotropic directional information from the point cloud, increase the number of

equations, and improve the performance. Figure 3 also demonstrates the improvement from the perspective of singular values. For a point cloud with 500 points, we can increase the number of equations to 1462 by choosing three different velocity vectors.

More velocity vectors would significantly increase the computational load while the marginal improvement also decreases. Therefore, we fix the number of velocity vectors $m = 3$ and solve the equation systems by using (13) in experiments.

4.2.3 Normal Estimation and Orientation. Orientation and surface reconstruction are closely related in computer graphics. Some proposed state-of-the-art methods (such as iPSR [Hou et al. 2022], PGR [Lin et al. 2023]) can balance orientation and reconstruction. Similarly, Our method can simultaneously accomplish the orientations and surface reconstruction tasks with state-of-the-art performance. As shown in (7), our method can output the points' unit outward normals by normalizing the **LSE** because the area element only determines the module length instead of the direction.

Firstly, we reshape μ into the matrix with the size of $N \times 3$, where each row represents an input point's normal information,

$$\mu \in \mathbb{R}^{3N \times 1} \rightarrow \hat{\mu} = \begin{bmatrix} \mu_1 & \mu_2 & \mu_3 \\ \vdots & \vdots & \vdots \\ \mu_{3N-2} & \mu_{3N-1} & \mu_{3N} \end{bmatrix} \in \mathbb{R}^{N \times 3}.$$

Then, we can complete the normal estimation and orientation of the point cloud by normalizing vectors row by row. Let \hat{n}_{p_i} be the estimated normal for point $p_i \in \mathcal{P}$,

$$\hat{n}_{p_i} = \frac{(\mu_{3i+1}, \mu_{3i+2}, \mu_{3i+3})}{\sqrt{\mu_{3i+1}^2 + \mu_{3i+2}^2 + \mu_{3i+3}^2}}.$$

Figures 8 and 12 show the qualitative comparison of normal estimation and orientation. Our method stimulates the potential for orientation in the Gauss formula by introducing anisotropy, especially for point clouds with thin structures or small holes. Our method achieves a high-quality, consistent orientation and the smaller deviation angle between the estimated normals and the ground truth, exhibiting superior results compared to other state-of-the-art methods.

4.2.4 Iso-surface Extraction. After obtaining μ , we compute the value of the indicator function on the query point set $Q = \{q_s\}_{s=1}^{N_Q}$, which is the set of all corner points on the octree, by the average of the matrices multiplication

$$\frac{1}{m} \sum_{i=1}^m A_{c_i}(Q; \mathcal{P}) \mu.$$

We follow previous works (i.e. [Kazhdan and Hoppe 2013], [Lu et al. 2019]) to extract surfaces with marching cubes on octrees. Note that the regularization term α in equation (13) or (16) may cause the iso-value's slight shift from $\frac{1}{2}$. We update the iso-value v_{iso} with

$$\begin{aligned} v_{\text{iso}} &= \text{average} \left(\frac{1}{m} \sum_{i=1}^m A_{c_i}(\mathcal{P}; \mathcal{P}) \mu \right) \\ &= \frac{1}{mN} \sum_{i=1}^m \sum_{j=1}^N A_{c_i}(p_j; \mathcal{P}) \mu. \end{aligned}$$

Our method can demonstrate the state-of-the-art performance of reconstruction from Figures 4, 6, and 10, which show the qualitative comparison of reconstructions with other well-known methods.

4.3 Adaptive Selection of Velocity Vectors

We select velocity vectors based on the singular value decomposition.

First, we select a subset \mathcal{P}_1 of the input point cloud \mathcal{P} for acceleration, calculate the geometric center $\mathbf{c} = (c_x, c_y, c_z)$ by

$$\mathbf{c} = \frac{1}{|\mathcal{P}_1|} \sum_{i=1}^{|\mathcal{P}_1|} \mathbf{p}_i,$$

and centralized points to $\mathbf{p}'_i = (p'_{i,x}, p'_{i,y}, p'_{i,z}), i = 1, 2, \dots, |\mathcal{P}_1|$, with

$$\mathbf{p}'_i = \mathbf{p}_i - \mathbf{c}.$$

Secondly, we can establish the corresponding covariance matrix

$$Cov = \frac{1}{|\mathcal{P}_1|} \sum_{i=1}^{|\mathcal{P}_1|} \begin{bmatrix} p'_{i,x} \cdot p'_{i,x} & p'_{i,x} \cdot p'_{i,y} & p'_{i,x} \cdot p'_{i,z} \\ p'_{i,y} \cdot p'_{i,x} & p'_{i,y} \cdot p'_{i,y} & p'_{i,y} \cdot p'_{i,z} \\ p'_{i,z} \cdot p'_{i,x} & p'_{i,z} \cdot p'_{i,y} & p'_{i,z} \cdot p'_{i,z} \end{bmatrix},$$

where $|\cdot|$ represents the number of elements in the set, and $Cov \in \mathbb{R}^{3 \times 3}$ is the symmetric matrix. Then, we can perform eigenvalue decomposition on the covariance matrix by spectral theorem

$$Cov = V \begin{bmatrix} \lambda_1 & & \\ & \lambda_2 & \\ & & \lambda_3 \end{bmatrix} V^T,$$

where $\lambda_1 \geq \lambda_2 \geq \lambda_3$. $V = (\mathbf{v}_1, \mathbf{v}_2, \mathbf{v}_3)^T$ is the matrix composed of the respective orthogonal eigenvectors, and the eigenvalues λ_i represent the degree of concentration of point cloud distribution in the corresponding direction \mathbf{v}_i .

Hence, \mathbf{v}_3 corresponds to the minimum eigenvalue's eigenvector and represents the plate's normal. In addition, we can determine the structural characteristics of point clouds by observing the eigenvalues λ_3 by the fact that the proximity of λ_3 to zero indicates a higher degree of thin structure within the corresponding point cloud.

Finally, based on the above analysis, we can complete the identification by whether it meets $\lambda_3 \leq \varepsilon$, where ε is a hyperparameter. Since the point cloud is standardized into the bounding box $[0, 1]^3$, ε is set to the constant 0.001 in the experiments in this article.

Then, the velocity field is chosen as follows.

$$\begin{cases} \mathbf{c}_1 = L \cdot \mathbf{v}_1, \mathbf{c}_2 = L \cdot \mathbf{v}_2, \mathbf{c}_3 = L \cdot \mathbf{v}_3, & \lambda_3 > \varepsilon \\ \mathbf{c}_1 = L \cdot \mathbf{v}_1, \mathbf{c}_2 = L \cdot \mathbf{v}_2, \mathbf{c}_3 = \frac{2\varepsilon L}{\lambda_3 + 0.1\varepsilon} \cdot \mathbf{v}_3, & \lambda_3 \leq \varepsilon, \end{cases}$$

where L is a given hyperparameter. The default value of L is 1.0, and the recommended setting range is 0.5 to 6. Algorithm 1 gives the detailed description of our method.

For point clouds with strong anisotropy, our method outperforms results as shown in Figures 7,6,8, and the supplementary materials.

5 EXPERIMENTS

Experimental Setup. Experiments are conducted using an NVIDIA GeForce RTX 3090 graphics card with 24GB video memory. The process of solving equations involves large matrix multiplications, for

Algorithm 1: Anisotropy-based Gauss Reconstruction

Data: Unoriented point cloud \mathcal{P} , maximum depth of octree D_{\max} , width function parameters w_{\min}, w_{\max} , regularization scaling factor α , batch size N_s , the modulus of velocity vectors L , the group of input velocity vectors $C = (\mathbf{c}_1, \mathbf{c}_2, \dots, \mathbf{c}_m)$.

Result: Oriented point cloud $(\mathcal{P}, \mathcal{N})$, a watertight surface M approximating the points.

- 1 Set up octree O of max depth D_{\max} by \mathcal{P} and obtain the corner points of the octree as query points \mathcal{Q} ;
 - 2 Compute the width of the input points as Lu et al. [2019];
 - 3 Calculate the eigenvalues $\lambda_1, \lambda_2, \lambda_3$ and corresponding eigenvectors of point clouds $\mathbf{v}_1, \mathbf{v}_2, \mathbf{v}_3$;
 - 4 Based on whether $\lambda_3 \leq 0.001$ to calculate velocity vectors $\mathbf{c}_{a_1}, \mathbf{c}_{a_2}, \mathbf{c}_{a_3}$ by adaptive strategy and decide whether to add to C . If added, $C \leftarrow C \cup \mathbf{c}_{a_1} \cup \mathbf{c}_{a_2} \cup \mathbf{c}_{a_3}$, $m \leftarrow m + 3$;
 - 5 **if** $m \leq 3$ **then**
 - 6 **for** $i = 1$ **to** m **do**
 - 7 Calculate matrix A_{c_i} by dividing rows into blocks based on batch size N_s , i.e.
 $A_{c_i} = (A_{c_{i,1}}, A_{c_{i,2}}, \dots, A_{c_{i,s}})^T$;
 - 8 **for** $j = 1$ **to** m **do**
 - 9 Calculate A_{c_j} by dividing rows into blocks similarly;
 - 10 Using Einstein summation to calculate $B_{i,j}$;
 - 11 **end**
 - 12 **end**
 - 13 Concatenate the complete matrix B and apply regularization $B \leftarrow B + (\alpha - 1) \cdot \text{diag}(B)$;
 - 14 Solve $B\xi = \frac{1}{2}$ for ξ by conjugate gradient(CG) algorithm;
 - 15 Calculate the linearized surface element $\mu = A^T \xi$ by Equation (13);
 - 16 **end**
 - 17 **if** $m \geq 3$ **then**
 - 18 **for** $i = 1$ **to** m **do**
 - 19 Calculate matrix A_{c_i} and $B \leftarrow B + A_{c_i}^T A_{c_i}$,
 $d \leftarrow d + A_{c_i}^T \frac{1}{2}$;
 - 20 **end**
 - 21 Concatenate the complete matrix B and apply regularization $B \leftarrow B + (\alpha - 1) \cdot \text{diag}(B)$;
 - 22 Calculate the linearized surface element μ with $B\mu = d$ by conjugate gradient(CG) algorithm;
 - 23 **end**
 - 24 Extract normals from μ and output oriented point cloud $(\mathcal{P}, \mathcal{N})$ Calculate the average coefficient matrix
 $\bar{A} = (\sum_{k=1}^m A_{c_k})/m$;
 - 25 Compute the iso-value as $v_{\text{iso}} = \text{average}(\bar{A}(\mathcal{P}; \mathcal{P})\mu)$;
 - 26 Obtain query points' values as $\bar{A}(\mathcal{Q}; \mathcal{P})\mu$;
 - 27 Reconstruct surface M using marching cubes by $\bar{A}(\mathcal{Q}; \mathcal{P})\mu$ and v_{iso} ;
-

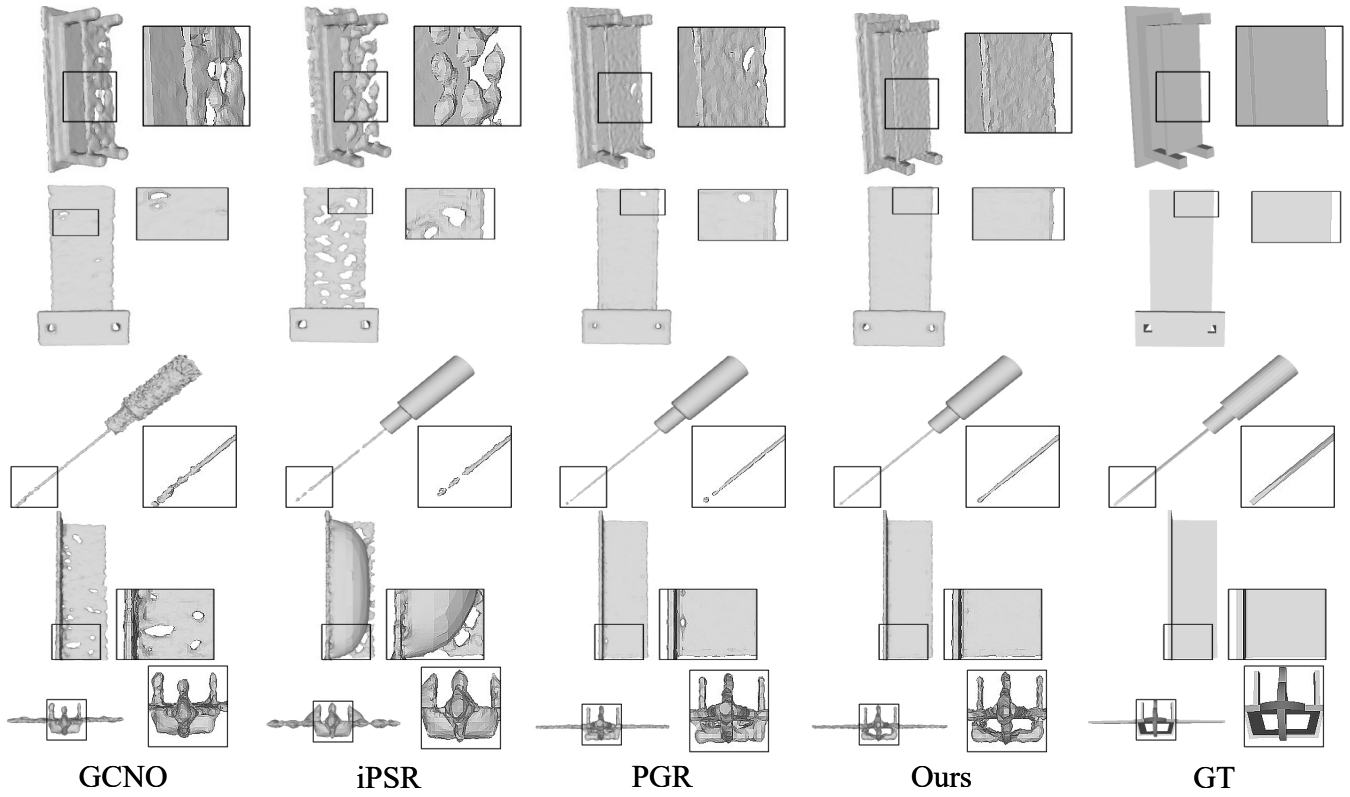


Fig. 6. Qualitative comparison of our method with other state-of-the-art methods on the reconstructions from point clouds with thin structure (the first, second, and fourth row), needle tip (the third row), or thin-walled space (the fifth row). Other state-of-the-art methods often fall into the issues, including sheet breakage, tip discontinuities, and wrong sealing. However, our method can handle these issues.

Models	PGP ₉₀ ↑					N_p ↑					N_s ↑					CD ↓				
	Ours	PGR	iPSR	GCNO	PCA	Ours	PGR	iPSR	GCNO	PCA	Ours	PGR	iPSR	GCNO	PCA	Ours	PGR	iPSR	GCNO	PCA
ABC00019908	0.9940	0.9930	0.9901	0.9736	0.8476	0.9288	0.9258	0.9265	0.8638	0.7486	0.9687	0.9662	0.9664	0.8376	0.7365	3.13	3.31	3.16	8.13	13.48
ABC00015485	1.0000	1.0000	1.0000	0.9930	0.9058	0.9621	0.9595	0.9527	0.9381	0.7911	0.9756	0.9740	0.9744	0.9238	0.7902	6.54	8.25	6.71	8.95	18.02
Trash_can20	0.9690	0.4975	0.5385	0.5200	0.5004	0.8378	0.1373	0.0722	0.0218	0.0036	0.7868	0.3179	0.0820	0.0809	0.0285	142.98	235.99	304.09	275.71	2654.13
Spoon5	1.0000	1.0000	0.9995	0.5336	0.5122	0.9563	0.9493	0.6066	0.0496	0.0181	0.9042	0.8169	0.7308	0.2336	0.0178	0.79	1.03	1.75	118.78	2996.84
Thing10k10218	0.9923	0.9919	0.9816	0.9434	0.8752	0.9330	0.9318	0.9234	0.8378	0.7205	0.9652	0.9553	0.9618	0.7964	0.8809	9.09	12.16	9.12	35.03	43.95
Screwdriver16	0.9804	0.9802	0.9793	0.7033	0.9504	0.9260	0.9250	0.9144	0.3627	0.8846	0.9563	0.9547	0.9510	0.6685	0.8331	1.82	1.97	1.89	2.76	53.74
Plate	1.0000	1.0000	1.0000	0.9998	0.5594	0.9575	0.9458	0.8659	0.9628	0.1321	0.9722	0.9644	0.9335	0.9750	0.0436	5.95	6.62	7.12	6.14	341.23
Thing10k16680	0.9966	0.9932	0.9965	0.6424	0.5093	0.9339	0.9095	0.9326	0.2229	0.0036	0.9661	0.9100	0.9639	0.5697	0.0586	15.69	54.78	16.11	282.61	1256.29
Thing10k88053	1.0000	1.0000	0.5595	0.9633	0.9891	0.9687	0.9597	0.1208	0.8927	0.9679	0.9815	0.8914	0.2227	0.7959	0.9548	3.88	10.89	19.38	7.68	49.38
Cup34	1.0000	0.9945	0.9995	0.8156	0.6636	0.9363	0.9282	0.9256	0.6147	0.3266	0.9830	0.7872	0.9586	0.6096	0.4307	13.35	300.74	16.44	142.59	254.35
Utah_teapot	0.9950	0.9845	0.9869	0.9920	0.9878	0.9499	0.9483	0.9438	0.9284	0.9439	0.9742	0.9711	0.9734	0.8895	0.9732	4.23	4.49	4.36	6.97	4.50
Thing10k132420	1.0000	1.0000	1.0000	1.0000	1.0000	0.9879	0.9852	0.9825	0.9679	0.9691	0.9900	0.9898	0.9882	0.9727	0.9702	0.96	0.97	0.98	0.97	1.61
Saxophone2	1.0000	1.0000	1.0000	0.6047	0.9332	0.9709	0.9702	0.9706	0.1359	0.8620	0.9840	0.9736	0.9813	0.1039	0.8099	1.12	1.18	1.46	4873.62	161.75
Average	0.9944	0.9573	0.9255	0.8219	0.7872	0.9422	0.8827	0.7798	0.5999	0.5670	0.9544	0.8825	0.8221	0.6505	0.5791	16.12	49.41	30.18	443.84	603.79

Table 1. Comparison of our method with other state-of-the-art methods for point clouds with 10K points on orientation and reconstruction. The CD values are multiplied by 10^5 . Our method exhibits superior performance against other state-of-the-art methods.

which we use Cupy [Nishino and Loomis 2017] for high-efficiency matrix computation on the GPU, like PGR.

Evaluating Indicator. The proportion of good points (PGP) is the ratio of points for which the angle between the estimated normal and its corresponding ground truth normal is smaller than a specified threshold. The higher value of PGP indicates better consistency in the orientation of the point cloud.

$$PGP_{90}(P) = |\text{correct}.P|/|P|, \text{correct}.P = \{p_i \in P | \mathbf{n}_{p_i, \text{out}} \cdot \mathbf{n}_{p_i, \text{true}} > 0\}.$$

The Chamfer distance (CD) penalizes both false negatives (missing parts) and false positives (excess parts) to evaluate the reconstruction error.

$$CD(S_1, S_2) = \frac{1}{|S_1|} \sum_{x \in S_1} \min_{y \in S_2} \|x - y\|_2^2 + \frac{1}{|S_2|} \sum_{y \in S_2} \min_{x \in S_1} \|x - y\|_2^2.$$

S_1 and S_2 denote the reconstructed and ground truth surfaces respectively. In the set in the subsection of evaluating indicators, $|\cdot|$ represents the number of elements. To evaluate the quality of

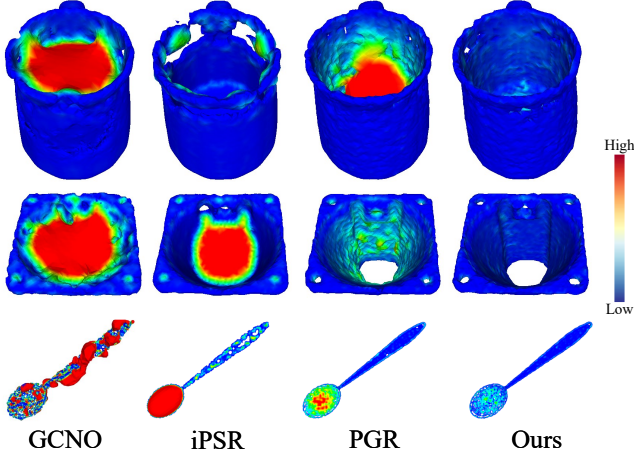


Fig. 7. Error colormaps of the cup in the Famous dataset, triangular pyramid in the Thingi10K dataset, and spoon in the Thin dataset. The colors in the figure represent the degree of error. Compared to the wrong sealing of other well-known methods, our method demonstrates state-of-the-art reconstruction performance.

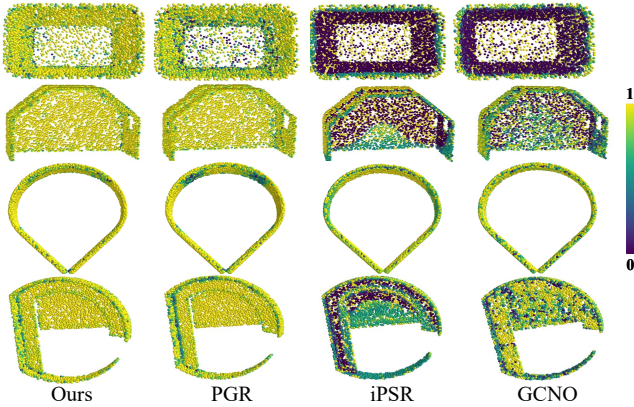


Fig. 8. Qualitative comparison of our method with other state-of-the-art methods about normal estimation. The color of the points represents the inner product of the estimated normals and the ground truth.

the reconstruction, we employ a sampling approach using 20,000 points for both surfaces.

Normal consistency (expressed as a percentage and abbreviated as ‘NC’) reflects the degree of normal consistency between two point clouds. The NC value is computed as follows:

$$NC(P_1, P_2) = \frac{1}{2|P_1|} \sum_{p_1 \in P_1} n_{p_1} n_{\text{closest}(p_1, P_2)} + \frac{1}{2|P_2|} \sum_{p_2 \in P_2} n_{p_2} n_{\text{closest}(p_2, P_1)}$$

$$\text{closest}(p, P) = \arg \min_{p' \in P} d(p, p'). \quad (17)$$

N_p means that P_1 is chosen as the ground truth of the input point cloud, and P_2 is the output oriented point cloud by the algorithm. As a supplement to PGP_{90} , it is mainly used to measure the algorithm’s ability of orientation and normal estimation.

Table 2. Quantitative comparisons of our method with other state-of-the-art methods on the orientation and reconstruction in the clean datasets. The CD values are multiplied by 10^5 . Our method demonstrates state-of-the-art performance.

		Real-world	Famous	ABC	Thingi10k
$PGP_{90} \uparrow$	GCNO	0.9537	0.9454	-	-
	iPSR	0.9747	0.9772	0.9128	0.9685
	PGR	0.9894	0.9776	0.9592	0.9859
	Ours	0.9914	0.9802	0.9661	0.9879
$NC_p \uparrow$	GCNO	0.7842	0.8196	-	-
	iPSR	0.8488	0.8447	0.7614	0.8646
	PGR	0.8893	0.8440	0.8370	0.8986
	Ours	0.8899	0.8487	0.8458	0.9011
$NC_s \uparrow$	GCNO	0.8244	0.8447	-	-
	iPSR	0.8852	0.8970	0.7883	0.8983
	PGR	0.9038	0.8779	0.8319	0.9122
	Ours	0.9193	0.8991	0.8660	0.9277
CD \downarrow	GCNO	41.38	36.83	-	-
	iPSR	28.02	21.77	45.18	18.10
	PGR	30.43	9.46	40.40	18.24
	Ours	25.90	8.30	15.86	12.23

Table 3. Quantitative comparisons of our method with other state-of-the-art methods on the orientation and reconstruction in the datasets with 0.5% Gaussian noise. The CD values are multiplied by 10^5 . Our method exhibits superior performance against other state-of-the-art methods in orientation and reconstruction.

		Real-world	Famous	ABC	Thingi10k
$PGP_{90} \uparrow$	GCNO	0.8864	0.9001	-	-
	iPSR	0.9411	0.9097	0.8487	0.9509
	PGR	0.9412	0.9346	0.9180	0.9487
	Ours	0.9427	0.9393	0.9216	0.9615
$NC_p \uparrow$	GCNO	0.7201	0.6875	-	-
	iPSR	0.7566	0.6908	0.6027	0.8108
	PGR	0.7343	0.7203	0.7109	0.8084
	Ours	0.7592	0.7241	0.7147	0.8168
$NC_s \uparrow$	GCNO	0.7795	0.8335	-	-
	iPSR	0.8587	0.8674	0.7586	0.8765
	PGR	0.9011	0.8773	0.7964	0.8766
	Ours	0.9137	0.8860	0.8347	0.8834
CD \downarrow	GCNO	61.38	39.68	-	-
	iPSR	73.38	22.96	46.65	19.64
	PGR	31.89	9.68	46.21	18.91
	Ours	26.28	8.46	19.18	12.71

N_s means that P_1 is sampled from the surface of the ground truth, P_2 is sampled from the output surface by the algorithm as a supplement to the Chamfer distance, it is mainly used to measure the algorithm’s ability of surface reconstruction.

Parameters. We adopt the parameter setting: $w_{\min} = 0.0015$, $L = 1.0$, $N_s = 5000$ in the experiments and use the CG algorithm

implemented in Python for solving the equation systems. We set the regularization term α to 1.2 – 2.0 for the clean point clouds and 2.0 – 5.0 for the noisy point clouds.

Baselines. We include three well-known and state-of-the-art (SOTA) methods (PGR [Lin et al. 2023], GCNO [Xu et al. 2023a], iPSR [Hou et al. 2022]) for comparison. For GCNO [Xu et al. 2023a], we follow the default setting and match it with SPR [Kazhdan and Hoppe 2013] for reconstruction. Due to the slow running speed of GCNO, we do not test its performance on large datasets. For PGR [Lin et al. 2023] and iPSR [Hou et al. 2022], besides experimenting with default parameters, we attempt to find the optimal parameters and display the optimal results. In most qualitative examples, our method adopts the same parameter values as PGR.

5.1 Experimental Effect

Famous, ABC and Thingi10K datasets. The Famous [Erlert et al. 2020] dataset includes dozens of classic shapes such as bunny, dragon, and armadillo. The ABC [Kingma and Ba 2014] dataset comprises a diverse collection of CAD meshes, while the Thingi10K [Zhou et al. 2022] dataset contains a variety of shapes with intricate geometric details. We randomly sample 5K points from each mesh. The quantitative comparison results of the methods and other well-known methods are shown in Table 2. We further tested our method’s ability and performance for dense point clouds that reflect the method’s ability to reconstruct the details of the structure. Table 1 shows the results compared with other well-known methods. The comparison of the qualitative results of normal estimation and orientation on these datasets is shown in Figure 8, while the comparison of qualitative results of surface reconstruction on these datasets is shown in Figures 4 and 7. Experimental results demonstrate the state-of-the-art performance of our method in these datasets.

Real-world Dataset. The Real-world [Hou et al. 2022] dataset contains noise and outliers from the scan. In addition, the ground truth exhibits lower smoothness. To verify the algorithm’s robustness, we utilize the Real-world dataset to generate point clouds with 5K points as input. The quantitative comparison results of the methods are shown in Table 2.

Noisy Datasets. The performance on noisy datasets can provide compelling evidence of the ability to handle variations and disturbances. However, most non-learning methods cannot handle noisy point clouds well, especially sparse point clouds. To evaluate this capability of our method, we introduce a uniform Gaussian noise of 0.5% to the Famous [Erlert et al. 2020], ABC [Kingma and Ba 2014], Thingi10K [Zhou et al. 2022] and Real-world [Hou et al. 2022] datasets with 5K points as input. The quantitative comparison results of our method and other well-known methods are shown in Table 3. Figure 9 displays the reconstructions from noisy point clouds. Numerous experiments showcase our method’s strong robustness and ability to reduce the noise’s interference on orientation and reconstruction.

Models with Holes. Models with holes are more complex and challenging to be dealt with, especially if the holes are narrow and deep. Although other methods have also paid attention to this issue

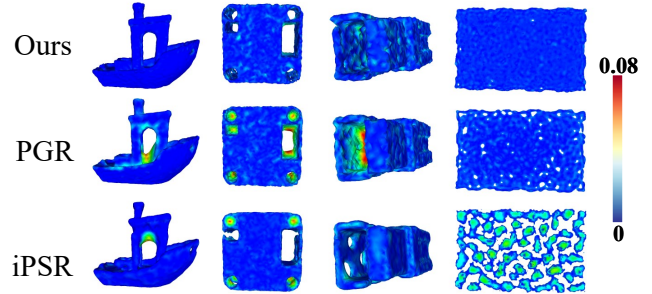


Fig. 9. Qualitative results of the reconstruction of noisy point clouds. Especially compared to PGR and iPSR, our method can better protect holes and avoid sealing them.

and worked very hard to address it, they still encounter the problem of sealing holes incorrectly when facing small or deep holes.

Thanks to the introduction of anisotropy and the ability to establish more non-homogeneous equations with the proposed novel adaptive directional selection strategy, our method can protect these precious details and output high-quality orientation and reconstruction with state-of-the-art performance, while PGR cannot work well under the same parameter values. Figures 10 and 12 show a qualitative comparison of reconstruction and orientation.

Thin Structures. As mentioned, thin structures often consist of two nearby surfaces with opposite normals. During normal estimation, the algorithm can be easily tricked into predicting the single surface’s normal and aligning the orientation of one surface with the other, which leads to poor results in both orientation and reconstruction. However, our method introduces anisotropy and provides a novel adaptive selection strategy for directional information based on the analysis of the thin structures. Figure 13 showcases our reconstruction of thin plates with a length and width of 0.25 only with a thickness between 0.012 and 0.025. Figures 6, 8, and Table 4 show the qualitative and quantitative comparisons of reconstruction results with other state-of-the-art methods. Our method can protect these valuable details with superior orientation and reconstruction for thin structures.

Sparse Point Clouds. Figure 3 shows the reconstruction of our method and PGR on a sparse point cloud with 500 points. Under the same parameter values, our method demonstrates superior reconstruction results compared to PGR, especially in continuity at the narrowed area.

Running Speed and Storage Complexity. The running speed of algorithm is also an important indicator. Figure 11 shows the time efficiency comparison of different reconstruction methods. Our method has a much faster computation speed than GCNO when handling point clouds ranging from 5K to 10K, and the overall time is similar to iPSR. Actually, For point clouds that are difficult to converge with, such as thin structures, the speed can be much faster than that of iPSR.

Nevertheless, we must admit that our method runs slower than PGR, although it is generally on the same order of magnitude. There are two main reasons for this: (1) we construct a larger number

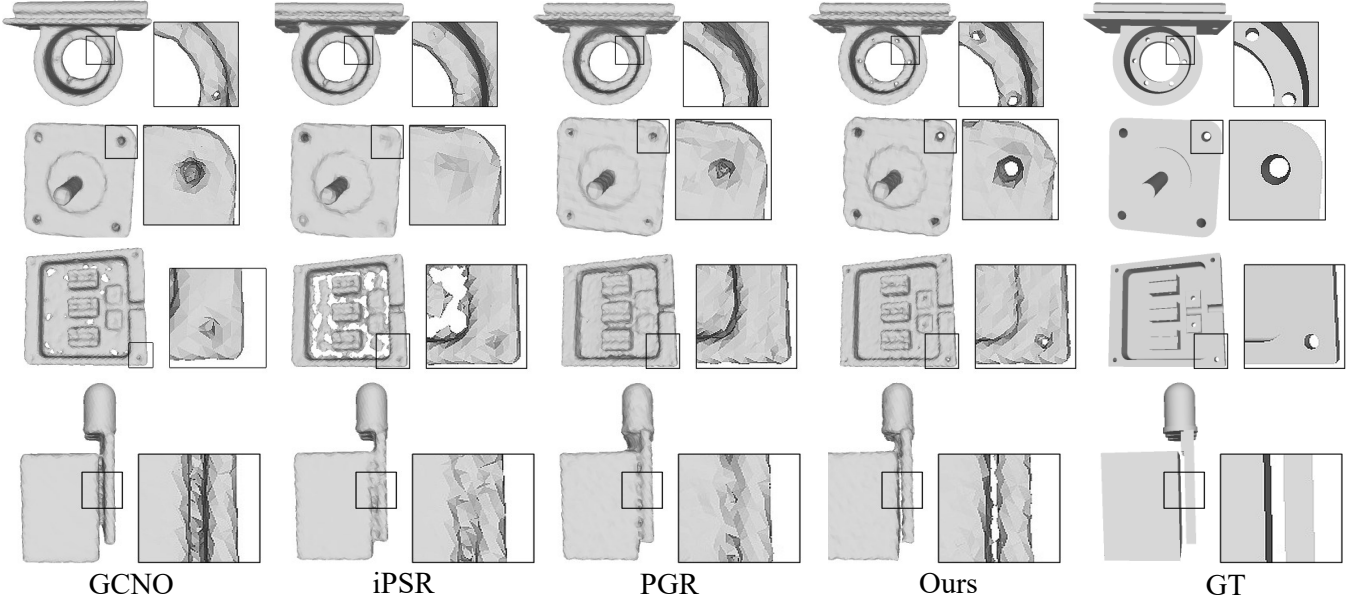


Fig. 10. Qualitative comparison of our method with other state-of-the-art methods on reconstruction for point clouds with holes or fine seams. PGR cannot handle small holes (first row), deep holes (second row), thin structure combined with small holes (third row), and narrow, thin seams (fourth row), like iPSR and GCNO. By introducing anisotropy, our method can protect these valuable details and output the good reconstructions.

Table 4. Quantitative comparisons of our method’s orientation and reconstruction under different length parameter L and regularization α on thin plates with a length and width of 0.5 and a thickness of 0.015 with other state-of-the-art methods under the same parameter values.

		PGP ₉₀ ↑	NC _p ↑	NC _s ↑	CD ↓
iPSR		0.9189	0.7853	0.7548	57.72
$\alpha=2$	PGR	0.9786	0.9167	0.8569	17.89
	Ours(L=0.5)	0.9834	0.9206	0.8743	8.75
	Ours(L=1)	0.9835	0.9207	0.8740	8.66
	Ours(L=3)	0.9848	0.9273	0.8784	8.09
	Ours(L=8)	0.9832	0.9193	0.8785	6.75
$\alpha=1.2$	PGR	0.9834	0.9168	0.8766	8.24
	Ours(L=0.5)	0.9845	0.9206	0.8797	7.16
	Ours(L=1)	0.9800	0.9185	0.8864	6.43
	Ours(L=3)	0.9728	0.9054	0.8783	6.84
	Ours(L=8)	0.9648	0.9037	0.8667	7.07

of equations, and (2) the analytical expression of the anisotropic fundamental solution and Gauss kernel function in our method is more complex. This is also the area where we need to improve and optimize further.

The comparison of running time between our method and other methods on point clouds of different scales is shown in Figure 11. Consistent with the previous theoretical analysis, our method requires a higher computational time than PGR due to the solving for the matrices with the size of $3N \times 3N$ instead of $N \times N$ in the experiment. Our method is slightly slower than iPSR with the

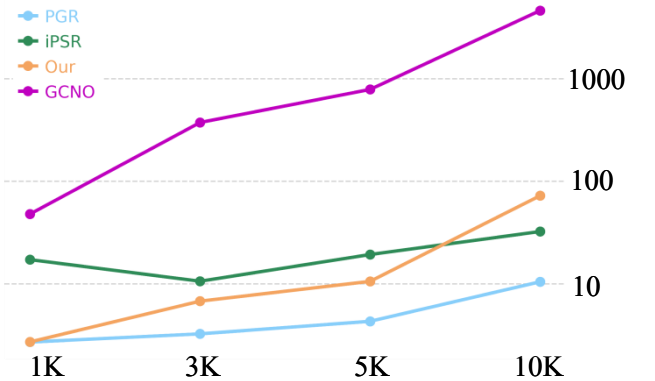


Fig. 11. Qualitative and visualized comparison of algorithms’ running time, where the y-coordinate uses logarithmic coordinates in seconds (/s). Our method can maintain the good running speed on the whole.

same order of magnitude when dealing with dense point clouds and significantly faster than GCNO.

The storage of $B = A_c A_c^T + (\alpha - 1) \cdot \text{diag}(A_c A_c^T)$ is the square of the number of input samples. This is also our bottleneck. This makes it hard for our method to handle point clouds with very large scale, just like PGR. In the experimental setting, we considered the case of $m = 3$. In contrast to PGR, which solves for the matrices with the size of $N \times N$, our approach involves solving for the matrices with the size of $3N \times 3N$. It is worth pointing out that although the

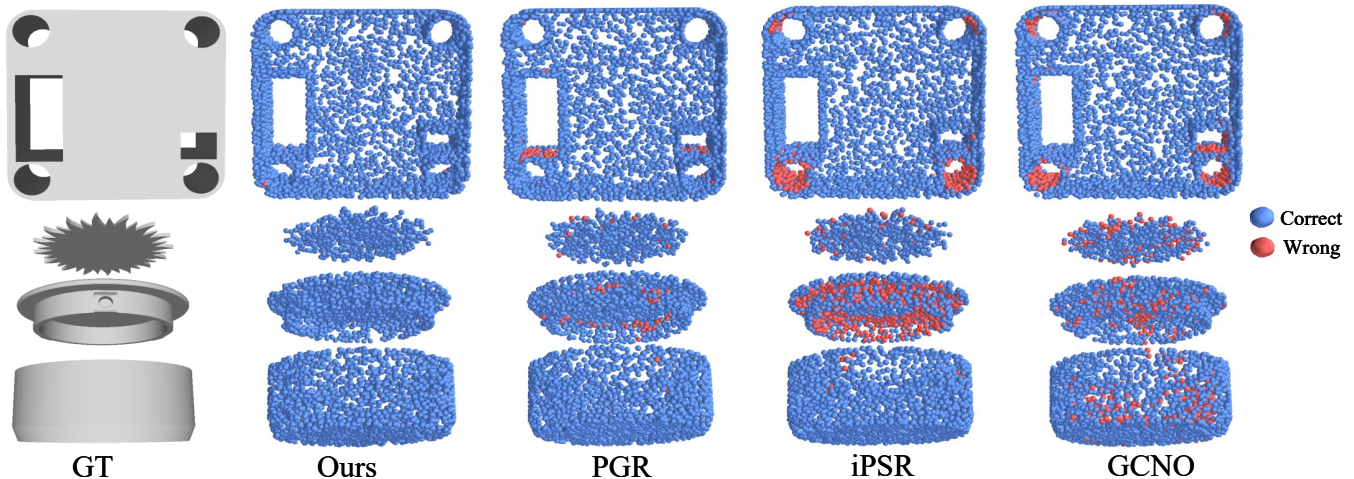


Fig. 12. Qualitative comparison of orientation. Existing state-of-the-art orientation approaches cannot deal with various tricky examples such as thin structures, holes, and sharp features. Note that the red points indicate the wrong orientation. Our method further explores the potential of the Gauss formula for orientation and displays superior performances compared to these methods.

maximum capacity of our method is about 1/9 of PGR in theory, the novel blocking matrix strategy we proposed improves it to be 1/3.

At present, our method has a computational complexity of $O(N^2)$ with the potential that the matrix-vector products $A_c \xi$ and $A_c^T \xi$ can be accelerated via the fast multipole method (FMM), ultimately reducing computational complexity to $O(N \log N)$.

5.2 Discussion of parameters

Module of Velocity Vectors. With the proposed novel adaptive selection strategy for velocity vectors, our method controls the number of hyperparameters and only adds the length parameter L to change the module of velocity vectors, compared to PGR. We conducted experiments to investigate the influence of length parameter L on normal estimation under different thicknesses D (0.003 - 0.008) of point clouds, as shown in Table 5. Within a certain range, combined with the adaptive selection strategy, increasing the value of length parameter L appropriately can improve the orientation quality of point clouds, especially for thin structures. Nevertheless, as the module of velocity vectors further increases, the corresponding truncation error will also increase due to the numerical approximation. Table 4 also show the quantitative comparisons of our method’s orientation and reconstruction under different length parameter L on thin plates. The recommended range of length parameter L is 0.5-6.

Table 5. The quantitative comparison of length parameter L on normal estimation under different thicknesses D (0.003 - 0.008) of point clouds.

$NC_p \uparrow$	0	0.5	1	2	4	6	8
0.008	0.8918	0.8970	0.9172	0.9194	0.9252	0.9248	0.9205
0.005	0.8471	0.8782	0.8873	0.8905	0.9036	0.9103	0.9018
0.004	0.8122	0.8564	0.8665	0.8739	0.8968	0.8976	0.8914
0.003	0.7942	0.8291	0.8439	0.8624	0.8810	0.8881	0.8802

Regularization. PGR often suffers from its sensitivity to regularization terms. Overall, the too-small α can lead to artifacts and a rough appearance in reconstruction. Excessive α can cause the deviation between minimal-norm equation(13) and the initial equation (12), resulting in two problems. The first is that the reconstructed surface is overly smooth, losing many details. The second is that the solved linear surface element leads to a decrease in the geometric meaning of the solution and the accuracy of orientation. Table 4 shows the orientation and reconstruction performance of our method and PGR under different levels of regularization. Thanks to anisotropy’s introduction, our method can perform better than PGR at any regularization level, to a certain extent. Figures 6,8 show the orientation and reconstruction results of our method and PGR under the same regularization parameters. Our method has lower sensitivity and dependence on regularization. The qualitative comparisons are also shown in the supplementary materials.

6 LIMITATION

However, our method still has shortcomings and room for improvement in the future.

The first limitation lies in the memory and running time. Although we have proposed a blocking matrix strategy to save memory, the current bottleneck is the computation and storage of coefficient matrices like PGR. Due to the increase in the number of equations, the maximum capacity of our method is about 1/3 of PGR, approximately 15K. Although our method’s speed is similar to iPSR and much faster than GCNO, it is slower than that of PGR due to establishing more equations, especially for the point clouds more than 10K.

The second limitation lies in the dependence and sensitivity of hyperparameters. Although we have significantly reduced the sensitivity and dependence on regularization terms α for solving the

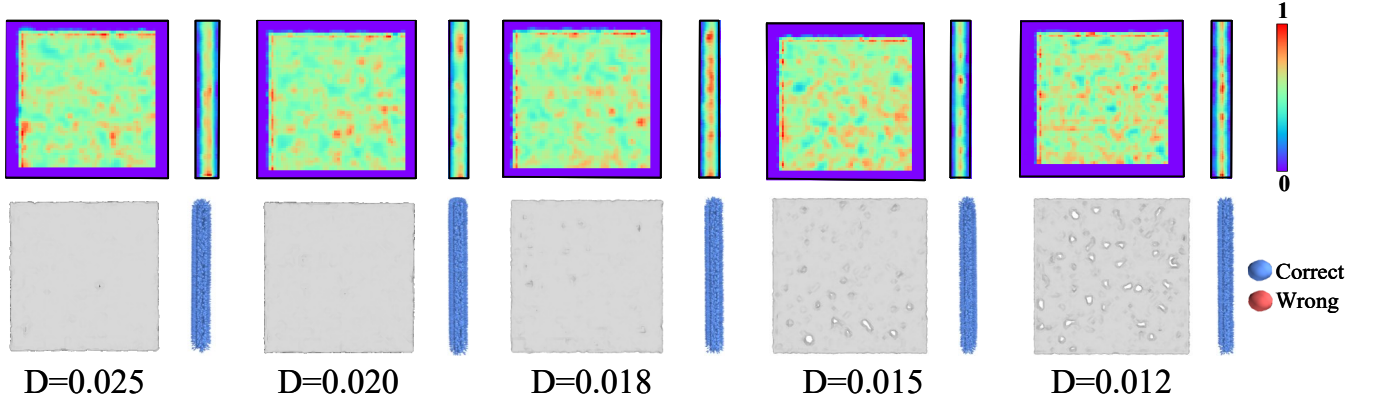


Fig. 13. The reconstruction and orientation of our method on thin plates with thickness D ranging from 0.012 to 0.025.

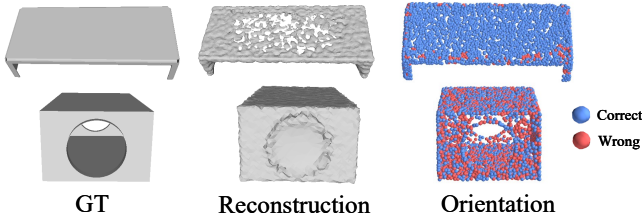


Fig. 14. Limitations of our method. The first row shows that our method can orient correctly for some thin structures while reconstructing them poorly. The second row shows the thin structures with holes that our method cannot orient and reconstruct well, just like PGR and iPSR.

equations, our method still cannot completely eliminate the dependence on regularization terms. The qualitative comparisons are shown in the supplementary materials.

In addition, introducing a convection term in the original Laplace operator makes the anisotropic Gauss formula more complex. This puts higher requirements on the hyperparameter w_{\min} , especially when the velocity vector's modulus is large. Excessive truncation may lead to a decrease in reconstruction performance. The truncation length w_{\min} is suggested to be set as 0.0015, which is also the default value of PGR.

In experiments, there are still some examples that our method cannot handle well. As shown in Figure 14, our method cannot deal with the orientation and reconstruction task of the sparse point clouds with thin structures and holes together well, just like other state-of-the-art methods. In addition, our method can improve the orientation for some difficult, thin structures but may show poor reconstruction performance. However, poor reconstruction is a common phenomenon. There still exists surface damage during reconstruction with the accurate values of the query points or taking the ground truth normals as the input.

7 FUTURE WORK

Our method still has many potentials worth exploring. In particular, the adaptive selection strategy for the velocity vector can be expanded in the following aspects.

Weighting Factor. We can further generalize the optimization problem (15) in the case of $m \geq 3$, highlighting the information through weighting factors η . In detail,

$$\min_{\mu} \sum_{i=1}^m \eta_i \|A_{c_i} \mu - d_i\|_2^2, \quad (18)$$

which can be computed as

$$H\mu = \left(\sum_{i=1}^m \eta_i A_{c_i}^T d_i \right), \quad \text{with } H = H_0 + \text{diag}(H_0), H_0 = \left(\sum_{i=1}^m \eta_i A_{c_i}^T A_{c_i} \right).$$

It is an effective way to highlight the anisotropic information and improve the results. For example, we can use an adaptive parameter selection strategy combined with $\eta_3 > 1$ to enhance the constraint on the thinnest direction further.

Point-wise Strategy. We have proposed the adaptive strategy for velocity vectors by using the overall features of the point cloud, which has good performance on thin structures. However, it has not fully stimulated the potential of our method.

As shown in the anisotropic Gauss formula (4), any velocity vector c can be used to calculate the indicator function. Compared to establishing a large number of equations through a unified velocity vector, we can tailor the velocity vector of each point in the anisotropic Gauss formula based on the characteristics of each input point cloud to utilize the local directional information.

The point cloud's local geometric features may not be consistent with the overall. Taking the surface composed of two perpendicular intersecting planes as an example, we tend to establish corresponding equations based on the correct normal of the point. However, using PCA on the whole point cloud can only estimate an overall normal. Hence, we propose a novel point-wise strategy by kNN and PCA at each point.

In detail, we further generalize \mathbf{c} in equation (9) to $\mathbf{c}_{\mathcal{P}_i}$,

$$A_i^{\mathcal{P}_i}(\mathcal{P}_i; \mathcal{P})\mu = \frac{1}{2}, \quad i = 1, 2, 3, \dots, N, \quad (19)$$

where $\mathcal{P}_i \in \mathcal{P}$ and $\mathbf{c}_{\mathcal{P}_i}$ can be obtained from the raw input cloud.

If there is more detailed information about point clouds, such as being composed of two thin planes, we can take the points with similar local features as a whole,

$$A_i^{\mathcal{P}_i}(\mathcal{P}_i; \mathcal{P})\mu = \frac{1}{2}, \quad (20)$$

where $\mathcal{P}_i \subset \mathcal{P}$. The point-wise strategy can not only avoid the increase in running time and memory but also improve the quality of the equations and reduce the singularity of matrix B .

8 CONCLUSION

This paper showcases our new research effort towards extending the fundamental solution into an anisotropic form and the derivation of the corresponding anisotropic Gauss formula in theory. Compared to the reconstruction based on the original Gauss formula, our method can construct more non-homogeneous equations by further utilizing the information on point clouds and anisotropy.

Furthermore, the introduction of anisotropy reduces our method's sensitivity to regularization parameters, improves the orientation, and enhances the algorithm's robustness. It significantly improves performance in the reconstruction of models with noise, holes, or thin structures. In response to the increasing number of equations, we propose numerical methods for solving under-determined and over-determined equation systems, respectively.

In addition, we have explored the selection of velocity vectors deeply and proposed the adaptive selection strategy by PCA and SVD. For thin structures, our proposed strategy selects the eigenvectors of the point cloud, and further improves the orientation and reconstruction performance.

Through extensive experiments, our approach shows superior performances in orientation and surface reconstruction compared to the other state-of-the-art methods.

REFERENCES

- Yizhak Ben-Shabat, Chamin Hewa Koneputugodage, and Stephen Gould. 2022. Digs: Divergence guided shape implicit neural representation for unoriented point clouds. In *Proceedings of the IEEE/CVF Conference on Computer Vision and Pattern Recognition*. 19323–19332.
- Fatih Calakli and Gabriel Taubin. 2011. SSD: Smooth signed distance surface reconstruction. In *Computer Graphics Forum*, Vol. 30. Wiley Online Library, 1993–2002.
- Eric Darve. 2000. The Fast Multipole Method: Numerical Implementation. *J. Comput. Phys.* 160, 1 (2000), 195–240. <https://doi.org/10.1006/jcph.2000.6451>
- Tamal K Dey and Jian Sun. 2005. . An Adaptive MLS Surface for Reconstruction with Guarantees. In *Symposium on Geometry processing*. 43–52.
- Philipp Erler, Paul Guerrero, Stefan Ohrhallinger, Niloy J Mitra, and Michael Wimmer. 2020. Points2surf learning implicit surfaces from point clouds. In *European Conference on Computer Vision*. Springer, 108–124.
- Amos Gropp, Lior Yariv, Niv Haim, Matan Atzmon, and Yaron Lipman. 2020. Implicit geometric regularization for learning shapes. *arXiv preprint arXiv:2002.10099* (2020).
- Paul Guerrero, Yanir Kleiman, Maks Ovsjanikov, and Niloy J Mitra. 2018. Pcpnet learning local shape properties from raw point clouds. In *Computer graphics forum*, Vol. 37. Wiley Online Library, 75–85.
- Hugues Hoppe, Tony DeRose, Tom Duchamp, John McDonald, and Werner Stuetzle. 1992. Surface reconstruction from unorganized points. In *Proceedings of the 19th annual conference on computer graphics and interactive techniques*. 71–78.
- Fei Hou, Chiyu Wang, Wencheng Wang, Hong Qin, Chen Qian, and Ying He. 2022. Iterative poisson surface reconstruction (ipstr) for unoriented points. *arXiv preprint arXiv:2209.09510* (2022).

- Zhiyang Huang, Nathan Carr, and Tao Ju. 2019. Variational implicit point set surfaces. *ACM Transactions on Graphics (TOG)* 38, 4 (2019), 1–13.
- Takashi Ijiri, Shin Yoshizawa, Yu Sato, Masaaki Ito, and Hideo Yokota. 2013. Bilateral Hermite Radial Basis Functions for Contour-based Volume Segmentation. In *Computer Graphics Forum*, Vol. 32. Wiley Online Library, 123–132.
- Michael Kazhdan. 2005. Reconstruction of solid models from oriented point sets. In *Proceedings of the third Eurographics symposium on Geometry processing*. 73–es.
- Michael Kazhdan, Matthew Bolitho, and Hugues Hoppe. 2006. Poisson surface reconstruction. In *Proceedings of the fourth Eurographics symposium on Geometry processing*, Vol. 7. 0.
- Misha Kazhdan, Ming Chuang, Szymon Rusinkiewicz, and Hugues Hoppe. 2020. Poisson surface reconstruction with envelope constraints. In *Computer graphics forum*, Vol. 39. Wiley Online Library, 173–182.
- Michael Kazhdan and Hugues Hoppe. 2013. Screened poisson surface reconstruction. *ACM Transactions on Graphics (ToG)* 32, 3 (2013), 1–13.
- Diederik P Kingma and Jimmy Ba. 2014. Adam: A method for stochastic optimization. *arXiv preprint arXiv:1412.6980* (2014).
- Ravikrishna Kolluri. 2008. Provably good moving least squares. *ACM Transactions on Algorithms (TALG)* 4, 2 (2008), 1–25.
- Qing Li, Huifang Feng, Kanle Shi, Yue Gao, Yi Fang, Yu-Shen Liu, and Zhizhong Han. 2023. Shs-net: Learning signed hyper surfaces for oriented normal estimation of point clouds. In *Proceedings of the IEEE/CVF Conference on Computer Vision and Pattern Recognition*. 13591–13600.
- Siyu Lin, Dong Xiao, Zuoqiang Shi, and Bin Wang. 2023. Surface Reconstruction from Point Clouds without Normals by Parametrizing the Gauss Formula. *ACM Trans. Graph.* 42, 2 (2023), 14:1–14:19.
- Shengjun Liu, Charlie CL Wang, Guido Brunnett, and Jun Wang. 2016. A closed-form formulation of HRBF-based surface reconstruction by approximate solution. *Computer-Aided Design* 78 (2016), 147–157.
- Wenja Lu, Zuoqiang Shi, Jian Sun, and Bin Wang. 2019. Surface Reconstruction Based on the Modified Gauss Formula. *ACM Trans. Graph.* 38, 1 (2019), 2:1–2:18.
- Ives Macêdo, Joao Paulo Gois, and Luiz Velho. 2011. Hermite radial basis functions implicit. In *Computer Graphics Forum*, Vol. 30. Wiley Online Library, 27–42.
- Josiah Manson, Gueergana Petrova, and Scott Schaefer. 2008. Streaming surface reconstruction using wavelets. In *Computer Graphics Forum*, Vol. 27. Wiley Online Library, 1411–1420.
- Margaret McIntyre and Grant Cairns. 1993. A new formula for winding number. *Geometriae Dedicata* 46, 2 (1993), 149–159.
- Gal Metzger, Rana Hanocka, Denis Zorin, Raja Giryes, Daniele Panozzo, and Daniel Cohen-Or. 2021. Orienting point clouds with dipole propagation. *ACM Transactions on Graphics (TOG)* 40, 4 (2021), 1–14.
- B.S. Morse, T.S. Yoo, P. Rheingans, D.T. Chen, and K.R. Subramanian. 2001. Interpolating implicit surfaces from scattered surface data using compactly supported radial basis functions. In *Proceedings International Conference on Shape Modeling and Applications*. 89–98. <https://doi.org/10.1109/SMA.2001.923379>
- ROYUD Nishino and Shohei Hido Crissman Loomis. 2017. Cupy: A numpy-compatible library for nvidia gpu calculations. *31st conference on neural information processing systems* 151, 7 (2017).
- Songyou Peng, Chiyu Jiang, Yiyi Liao, Michael Niemeyer, Marc Pollefeys, and Andreas Geiger. 2021. Shape as points: A differentiable poisson solver. *Advances in Neural Information Processing Systems* 34 (2021), 13032–13044.
- Xiaohua Ren, Luan Lyu, Xiaowei He, Wei Cao, Zhixian Yang, Bin Sheng, Yanci Zhang, and Enhua Wu. 2018. Biorthogonal wavelet surface reconstruction using partial integrations. In *Computer Graphics Forum*, Vol. 37. Wiley Online Library, 13–24.
- Christian Walder, Olivier Chapelle, and Bernhard Schölkopf. 2006. Implicit surfaces with globally regularised and compactly supported basis functions. *Advances in Neural Information Processing Systems* 19 (2006).
- Zixiong Wang, Yunxiao Zhang, Rui Xu, Fan Zhang, Peng-Shuai Wang, Shuangmin Chen, Shiqing Xin, Wenping Wang, and Changhe Tu. 2023. Neural-Singular-Hessian: Implicit Neural Representation of Unoriented Point Clouds by Enforcing Singular Hessian. *ACM Transactions on Graphics (TOG)* 42, 6 (2023), 1–14.
- Dong Xiao, Zuoqiang Shi, Siyu Li, Bailin Deng, and Bin Wang. 2023. Point normal orientation and surface reconstruction by incorporating isovalue constraints to Poisson equation. *Computer Aided Geometric Design* 103 (2023), 102195.
- Rui Xu, Zhiyang Dou, Ningna Wang, Shiqing Xin, Shuang-Min Chen, Mingyan Jiang, Xiaohu Guo, Wenping Wang, and Changhe Tu. 2023a. Globally Consistent Normal Orientation for Point Clouds by Regularizing the Winding-Number Field. *ACM Trans. Graph.* 42, 4 (2023), 111:1–111:15.
- Rui Xu, Zhiyang Dou, Ningna Wang, Shiqing Xin, Shuangmin Chen, Mingyan Jiang, Xiaohu Guo, Wenping Wang, and Changhe Tu. 2023b. Globally consistent normal orientation for point clouds by regularizing the winding-number field. *ACM Transactions on Graphics (TOG)* 42, 4 (2023), 1–15.
- Junsheng Zhou, Baorui Ma, Yu-Shen Liu, Yi Fang, and Zhizhong Han. 2022. Learning consistency-aware unsigned distance functions progressively from raw point clouds. *Advances in Neural Information Processing Systems* 35 (2022), 16481–16494.

A DERIVATION OF ISOTROPIC FUNDAMENTAL SOLUTIONS

The fundamental solution of n -dimensions has the generalized analytical formula

$$\Phi(\mathbf{x}) = \begin{cases} -\frac{1}{2\pi} \log|\mathbf{x}|, & n = 2 \\ \frac{1}{n(n-2)\omega(n)} \frac{1}{|\mathbf{x}|^{n-2}}, & n \geq 3 \end{cases} \quad (21)$$

of the original Laplace equation $\Delta u = 0$. Where $\omega(n)$ is the volume of a n -dimensional unit sphere, namely $\omega(n) = \pi^{\frac{n}{2}} / \Gamma(\frac{n}{2} + 1)$, and $\Gamma(\cdot)$ is the Gamma function.

Firstly, we utilize symmetry to search for its radial solution, treating it as a function of $r = |\mathbf{x}|$, which is only related to the length of the \mathbf{x} . Suppose that $u(\mathbf{x}) = v(r)$, $\mathbf{x} = (x_1, x_2, x_3, \dots, x_n)$, then

$$u_{x_i} = v'(r) \frac{x_i}{r}, u_{x_i x_i} = v''(r) \frac{x_i^2}{r^2} + v'(r) \left(\frac{1}{r} - \frac{x_i^2}{r^3} \right), \quad i = 1, 2, \dots, n.$$

Thus

$$\begin{aligned} \Delta u &= v''(r) \frac{x_1^2 + x_2^2 + x_3^2 + \dots + x_n^2}{r^2} + v'(r) \left(\frac{n}{r} - \frac{x_1^2 + x_2^2 + x_3^2 + \dots + x_n^2}{r^3} \right) \\ &= v''(r) + v'(r) \left(\frac{n-1}{r} \right). \end{aligned}$$

Due to $\Delta u = 0$, then

$$v''(r) + v'(r) \left(\frac{n-1}{r} \right) = 0.$$

This is a second-order ordinary differential equation (ODE) about scalar r . When $n \geq 3$, it can be solved by quadratic integration. We can also solve it by using the method of constant variation, assuming that it has the form of $v = r^m$.

B DERIVATION OF ANISOTROPIC FUNDAMENTAL SOLUTIONS

This is the calculation process of Equation (3).

Due to the addition of velocity vector \mathbf{c} , the generalized Laplace equation (3) may not have symmetry, so it cannot be simply processed according to the previous method of solving isotropic equations. Firstly, let

$$u(\mathbf{x}) = v(\mathbf{x}) e^{\frac{1}{2} \mathbf{c} \cdot \mathbf{x}},$$

then

$$\begin{aligned} \nabla u(\mathbf{x}) &= \nabla(v(\mathbf{x}) e^{\frac{1}{2} \mathbf{c} \cdot \mathbf{x}}) \\ &= e^{\frac{1}{2} \mathbf{c} \cdot \mathbf{x}} \nabla v(\mathbf{x}) + v(\mathbf{x}) \cdot \frac{1}{2} \mathbf{c} e^{\frac{1}{2} \mathbf{c} \cdot \mathbf{x}}. \end{aligned}$$

Naturally,

$$\begin{aligned} \Delta u(\mathbf{x}) &= e^{\frac{1}{2} \mathbf{c} \cdot \mathbf{x}} \Delta v(\mathbf{x}) + \frac{1}{2} e^{\frac{1}{2} \mathbf{c} \cdot \mathbf{x}} \mathbf{c} \cdot \nabla v(\mathbf{x}) + e^{\frac{1}{2} \mathbf{c} \cdot \mathbf{x}} \frac{1}{2} \mathbf{c} \cdot \nabla v(\mathbf{x}) + \frac{1}{4} |\mathbf{c}|^2 e^{\frac{1}{2} \mathbf{c} \cdot \mathbf{x}} \\ &= e^{\frac{1}{2} \mathbf{c} \cdot \mathbf{x}} \Delta v(\mathbf{x}) + e^{\frac{1}{2} \mathbf{c} \cdot \mathbf{x}} \mathbf{c} \cdot \nabla v(\mathbf{x}) + \frac{1}{4} |\mathbf{c}|^2 e^{\frac{1}{2} \mathbf{c} \cdot \mathbf{x}}, \end{aligned}$$

and

$$\begin{aligned} 0 &= \Delta u - \mathbf{c} \cdot \nabla u = e^{\frac{1}{2} \mathbf{c} \cdot \mathbf{x}} \Delta v(\mathbf{x}) + e^{\frac{1}{2} \mathbf{c} \cdot \mathbf{x}} \mathbf{c} \cdot \nabla v(\mathbf{x}) + \frac{1}{4} |\mathbf{c}|^2 e^{\frac{1}{2} \mathbf{c} \cdot \mathbf{x}} \\ &\quad - \mathbf{c} \cdot (e^{\frac{1}{2} \mathbf{c} \cdot \mathbf{x}} \nabla v(\mathbf{x}) + v(\mathbf{x}) \cdot \frac{1}{2} \mathbf{c} e^{\frac{1}{2} \mathbf{c} \cdot \mathbf{x}}) \\ &= e^{\frac{1}{2} \mathbf{c} \cdot \mathbf{x}} (\Delta v(\mathbf{x}) - \frac{1}{4} |\mathbf{c}|^2 v(\mathbf{x})). \end{aligned}$$

Hence, we can get

$$\Delta v(\mathbf{x}) - \frac{1}{4} |\mathbf{c}|^2 v(\mathbf{x}) = 0, \quad (22)$$

and let $k^2 = \frac{1}{4} |\mathbf{c}|^2$. Since the equation (22) is radial symmetric, we can suppose that $v(\mathbf{x}) = w(r)$, $r = |\mathbf{x}|$,

$$\Delta v(\mathbf{x}) = w''(r) + \frac{2}{r} w'(r),$$

then

$$w''(r) + \frac{2}{r} w'(r) - k^2 w(r) = 0. \quad (23)$$

At this point, we let

$$w(r) = e^{kr} \bar{w}(r), \quad k = \pm \frac{1}{2} |\mathbf{c}|,$$

then we can get

$$\begin{aligned} w'(r) &= e^{kr} (k \bar{w}(r) + \bar{w}'(r)), \\ w''(r) &= e^{kr} (\bar{w}''(r) + 2k \bar{w}'(r) + k^2 \bar{w}(r)). \end{aligned}$$

Furthermore, put these into equation (23), then

$$0 = w''(r) + \frac{2}{r} w'(r) - k^2 w(r) = e^{kr} (\bar{w}''(r) + 2k \bar{w}'(r) + \frac{2}{r} \bar{w}'(r) + \frac{2k}{r} \bar{w}(r)).$$

In other words,

$$\bar{w}''(r) + 2k \bar{w}'(r) + \frac{2}{r} \bar{w}'(r) + \frac{2k}{r} \bar{w}(r) = 0. \quad (24)$$

Finally, we can obtain the analytical solution of equation (24) using the method of constant variation.

$$\bar{w}(r) = \frac{s}{r},$$

where s is a constant. Hence,

$$\begin{aligned} v(r) &= e^{kr} \frac{s}{r}, \\ u(\mathbf{x}) &= \frac{s}{|\mathbf{x}|} e^{\frac{1}{2} (\mathbf{c} \cdot \mathbf{x} - |\mathbf{c}| |\mathbf{x}|)}. \end{aligned}$$

Since the fundamental solution of the generalized equation is related to the constant \mathbf{c} , we denote these fundamental solutions as $\Phi_{\mathbf{c}}(\mathbf{x})$.

Due to the natural degradation of $\Phi_{\mathbf{c}}(\mathbf{x})$ to $\Phi(\mathbf{x})$ when $\mathbf{c} = (0, 0, 0)^T$, hence, we can get $s = \frac{1}{4\pi}$, in other words,

$$\Phi_{\mathbf{c}}(\mathbf{x}) = \frac{1}{4\pi |\mathbf{x}|} e^{\frac{1}{2} (\mathbf{c} \cdot \mathbf{x} - |\mathbf{c}| |\mathbf{x}|)}. \quad \blacksquare$$

C DERIVATION OF ANISOTROPIC GAUSS FORMULA

This is the proof process of Theorem 1.

We will prove the theorem in three different situations $\mathbf{x} \in \Omega$, $\mathbf{x} \in \partial\Omega$ and $\mathbf{x} \in \overline{\Omega}^c$, where $\overline{\Omega}^c$ represents the complement of the closure of Ω .

First, for $\mathbf{x} \in \overline{\Omega}^c$, by using the divergence theorem and the fact that $\Phi_{\mathbf{c}}$ is smooth for $\mathbf{y} \in \Omega$, $\mathbf{x} \in \overline{\Omega}^c$,

$$\begin{aligned} & \int_{\partial\Omega} K_{\mathbf{c}}(\mathbf{x} - \mathbf{y}) \cdot \mathbf{n}(\mathbf{y}) dS(\mathbf{y}) \\ &= \int_{\partial\Omega} (\nabla\Phi_{\mathbf{c}} - \mathbf{c} \cdot \Phi_{\mathbf{c}})(\mathbf{x} - \mathbf{y}) \cdot \mathbf{n}(\mathbf{y}) dS(\mathbf{y}) \\ &= \int_{\Omega} (\Delta\Phi_{\mathbf{c}} - \mathbf{c} \cdot \nabla\Phi_{\mathbf{c}}) d\mathbf{y} \\ &= \int_{\Omega} 0 d\mathbf{y} = 0. \end{aligned}$$

In other words, $\forall \mathbf{c}, \forall \mathbf{x} \in \overline{\Omega}^c$,

$$\int_{\partial\Omega} K_{\mathbf{c}}(\mathbf{x} - \mathbf{y}) \cdot \mathbf{n}(\mathbf{y}) dS(\mathbf{y}) = 0.$$

Secondly, for $\mathbf{x} \in \Omega$, $\Phi_{\mathbf{c}}(\mathbf{x} - \mathbf{y})$ is not smooth for all $\mathbf{x} \in \Omega$. In order to overcome this problem, we fix $\varepsilon > 0$ sufficiently small such that $B(\mathbf{x}; \varepsilon)$ which is the ball with \mathbf{x} as the center and $\varepsilon > 0$ as the radius is contained within Ω . Then on the region $\Omega - B(\mathbf{x}; \varepsilon)$, $\Phi_{\mathbf{c}}(\mathbf{x} - \mathbf{y})$ is smooth and we can obtain that

$$\begin{aligned} 0 &= \int_{\Omega - B(\mathbf{x}; \varepsilon)} \Delta\Phi_{\mathbf{c}} - \mathbf{c} \cdot \nabla\Phi_{\mathbf{c}} d\mathbf{y} \\ &= \int_{\partial\Omega - \partial B(\mathbf{x}; \varepsilon)} (\nabla\Phi_{\mathbf{c}} - \mathbf{c} \cdot \Phi_{\mathbf{c}})(\mathbf{x} - \mathbf{y}) \cdot \mathbf{n}(\mathbf{y}) dS(\mathbf{y}) \\ &= \int_{\partial\Omega} (\nabla\Phi_{\mathbf{c}} - \mathbf{c} \cdot \Phi_{\mathbf{c}})(\mathbf{x} - \mathbf{y}) \cdot \mathbf{n}(\mathbf{y}) dS(\mathbf{y}) \\ &+ \int_{\partial B(\mathbf{x}; \varepsilon)} (\nabla\Phi_{\mathbf{c}} - \mathbf{c} \cdot \Phi_{\mathbf{c}})(\mathbf{x} - \mathbf{y}) \cdot \mathbf{n}_B(\mathbf{y}) dS(\mathbf{y}), \end{aligned}$$

where \mathbf{n}_B is the outer unit normal to $B(\mathbf{x}; \varepsilon)$, which is given by

$$\mathbf{n}_B(\mathbf{y}) = \frac{\mathbf{x} - \mathbf{y}}{|\mathbf{x} - \mathbf{y}|} \triangleq \frac{\mathbf{r}}{|\mathbf{r}|},$$

for $\mathbf{y} \in \partial B(\mathbf{x}; \varepsilon)$. Denote

$$F(\mathbf{c}, \varepsilon) = \int_{\partial B(\mathbf{x}; \varepsilon)} (\nabla\Phi_{\mathbf{c}} - \mathbf{c} \cdot \Phi_{\mathbf{c}})(\mathbf{x} - \mathbf{y}) \cdot \mathbf{n}_B(\mathbf{y}) dS(\mathbf{y}).$$

On the one hand $\forall \mathbf{c}$,

$$\begin{aligned} F(\mathbf{c}, \varepsilon) &= \int_{\partial B(\mathbf{x}; \varepsilon)} \frac{1}{4\pi|\mathbf{r}|} e^{1/2(\mathbf{c} \cdot \mathbf{r} - |\mathbf{c}||\mathbf{r}|)} \left(-\frac{\mathbf{r}}{|\mathbf{r}|^2} - \frac{1}{2}\mathbf{c} - \frac{1}{2}|\mathbf{c}|\frac{\mathbf{r}}{|\mathbf{r}|}\right) \cdot \frac{\mathbf{r}}{|\mathbf{r}|} dS(\mathbf{y}) \\ &= \int_{\partial B(\mathbf{x}; \varepsilon)} \frac{1}{4\pi|\mathbf{r}|} e^{1/2(\mathbf{c} \cdot \mathbf{r} - |\mathbf{c}||\mathbf{r}|)} \left(-\frac{1}{|\mathbf{r}|} - \frac{\mathbf{c} \cdot \mathbf{r}}{2|\mathbf{r}|} - \frac{1}{2}|\mathbf{c}|\right) dS(\mathbf{y}) \\ &\leq \int_{\partial B(\mathbf{x}; \varepsilon)} \frac{1}{4\pi|\mathbf{r}|} e^{1/2(-|\mathbf{c}||\mathbf{r}| - |\mathbf{c}||\mathbf{r}|)} \left(-\frac{1}{|\mathbf{r}|} - \frac{\mathbf{c} \cdot \mathbf{r}}{2|\mathbf{r}|} - \frac{1}{2}|\mathbf{c}|\right) dS(\mathbf{y}) \\ &= \int_{\partial B(\mathbf{x}; \varepsilon)} \frac{1}{4\pi|\mathbf{r}|} e^{(-|\mathbf{c}||\mathbf{r}|)} \left(-\frac{1}{|\mathbf{r}|} - \frac{\mathbf{c} \cdot \mathbf{r}}{2|\mathbf{r}|} - \frac{1}{2}|\mathbf{c}|\right) dS(\mathbf{y}) \\ &\leq \int_{\partial B(\mathbf{x}; \varepsilon)} \frac{1}{4\pi|\mathbf{r}|} e^{(-|\mathbf{c}||\mathbf{r}|)} \left(-\frac{1}{|\mathbf{r}|} + \frac{|\mathbf{c}||\mathbf{r}|}{2|\mathbf{r}|} - \frac{1}{2}|\mathbf{c}|\right) dS(\mathbf{y}) \\ &\leq \int_{\partial B(\mathbf{x}; \varepsilon)} \frac{1}{4\pi|\mathbf{r}|} e^{(-|\mathbf{c}||\mathbf{r}|)} \left(-\frac{1}{|\mathbf{r}|}\right) dS(\mathbf{y}) \\ &= \frac{1}{4\pi|\mathbf{r}|} e^{(-|\mathbf{c}||\mathbf{r}|)} \left(-\frac{1}{|\mathbf{r}|}\right) \int_{\partial B(\mathbf{x}; \varepsilon)} dS(\mathbf{y}) \\ &= -e^{(-|\mathbf{c}||\mathbf{r}|)} = -e^{(-|\mathbf{c}|\varepsilon)} \triangleq F_1(\mathbf{c}, \varepsilon). \end{aligned}$$

On the other hand $\forall \mathbf{c}$,

$$\begin{aligned} F(\varepsilon) &\geq \int_{\partial B(\mathbf{x}; \varepsilon)} \frac{1}{4\pi|\mathbf{r}|} e^{1/2(|\mathbf{c}||\mathbf{r}| - |\mathbf{c}||\mathbf{r}|)} \left(-\frac{1}{|\mathbf{r}|} - \frac{\mathbf{c} \cdot \mathbf{r}}{2|\mathbf{r}|} - \frac{1}{2}|\mathbf{c}|\right) dS(\mathbf{y}) \\ &= \int_{\partial B(\mathbf{x}; \varepsilon)} \frac{1}{4\pi|\mathbf{r}|} \left(-\frac{1}{|\mathbf{r}|} - \frac{\mathbf{c} \cdot \mathbf{r}}{2|\mathbf{r}|} - \frac{1}{2}|\mathbf{c}|\right) dS(\mathbf{y}) \\ &\geq \int_{\partial B(\mathbf{x}; \varepsilon)} \frac{1}{4\pi|\mathbf{r}|} \left(-\frac{1}{|\mathbf{r}|} - \frac{|\mathbf{c}||\mathbf{r}|}{2|\mathbf{r}|} - \frac{1}{2}|\mathbf{c}|\right) dS(\mathbf{y}) \\ &= \frac{1}{4\pi|\mathbf{r}|} \left(-\frac{1}{|\mathbf{r}|} - |\mathbf{c}|\right) \int_{\partial B(\mathbf{x}; \varepsilon)} dS(\mathbf{y}) \\ &= -1 - |\mathbf{c}|\varepsilon = -1 - |\mathbf{c}|\varepsilon \triangleq F_2(\mathbf{c}, \varepsilon). \end{aligned}$$

Letting the fixed $\varepsilon \rightarrow 0^+$, then we can find that

$$\lim_{\varepsilon \rightarrow 0^+} F_1(\mathbf{c}, \varepsilon) = -1, \quad \lim_{\varepsilon \rightarrow 0^+} F_2(\mathbf{c}, \varepsilon) = -1.$$

Therefore, it can be inferred from the squeeze theorem that

$$\lim_{\varepsilon \rightarrow 0^+} F(\mathbf{c}, \varepsilon) = -1.$$

In other words, $\forall \mathbf{c}, \forall \mathbf{x} \in \Omega$,

$$\int_{\partial\Omega} K_{\mathbf{c}}(\mathbf{x} - \mathbf{y}) \cdot \mathbf{n}(\mathbf{y}) dS(\mathbf{y}) = 1.$$

Last, we consider the case $\mathbf{x} \in \partial\Omega$. In this case, $\Phi_{\mathbf{c}}(\mathbf{x} - \mathbf{y})$ is not defined at $\mathbf{y} = \mathbf{x}$. Fix $\mathbf{x} \in \partial\Omega$. Let $B(\mathbf{x}; \varepsilon)$ be the ball of radius r about \mathbf{x} . Let $\Omega_{\varepsilon} \equiv \Omega - (\Omega \cap B(\mathbf{x}; \varepsilon))$, and $C_{\varepsilon} \equiv \{\mathbf{y} \in \partial B(\mathbf{x}; \varepsilon) : \mathbf{n} \cdot \mathbf{y} < 0\}$, and $\widetilde{C}_{\varepsilon} \equiv \partial\Omega_{\varepsilon} \cap C_{\varepsilon}$.

Firstly, we provide a lemma that needs to be used and provide the proof of it.

LEMMA 2. For $\widetilde{C}_{\varepsilon}$ and C_{ε} as defined above, we have

$$\int_{\widetilde{C}_{\varepsilon}} dS(\mathbf{y}) = \int_{C_{\varepsilon}} dS(\mathbf{y}) + O(\varepsilon^3).$$

We just need to show that the surface area of $\widetilde{C}_{\varepsilon} - C_{\varepsilon}$ is $O(\varepsilon^3)$. The surface area is approximately the surface area of the base times the height. Now the surface area of the base is $O(\varepsilon)$. Therefore, we just need to show that the height is $O(\varepsilon^2)$.

Without loss of generality, we let $\mathbf{x} = \mathbf{0}$. Now, by assumption, $\partial\Omega$ is C^2 . Therefore, $\partial\Omega$ can be written as the graph of a C^2 function $f: \mathbb{R}^2 \rightarrow \mathbb{R}$ such that $f(\mathbf{0}) = 0$ and $\nabla f(\mathbf{0}) = \mathbf{0}$. Therefore, if $\mathbf{y} = (y_1, y_2, y_3) \in C_\varepsilon - \overline{C_\varepsilon}$, then

$$|y_3| \leq |f(y_1, y_2)| \leq C|(y_1, y_2)|^2 \leq C\varepsilon^2,$$

by using Taylor's theorem. Therefore, the height is $O(\varepsilon^2)$ and the lemma follows.

Then, we start to prove this situation. First, we note that

$$\begin{aligned} 0 &= \int_{\Omega_\varepsilon} \Delta\Phi_c - \mathbf{c} \cdot \nabla\Phi_c d\mathbf{y} \\ &= \int_{\partial\Omega_\varepsilon} (\nabla\Phi_c - \mathbf{c} \cdot \Phi_c)(\mathbf{x} - \mathbf{y}) \cdot \mathbf{n}(\mathbf{y}) dS(\mathbf{y}) \\ &= \int_{\partial\Omega_\varepsilon - \overline{C_\varepsilon}} (\nabla\Phi_c - \mathbf{c} \cdot \Phi_c)(\mathbf{x} - \mathbf{y}) \cdot \mathbf{n}(\mathbf{y}) dS(\mathbf{y}) \\ &\quad + \int_{\overline{C_\varepsilon}} (\nabla\Phi_c - \mathbf{c} \cdot \Phi_c)(\mathbf{x} - \mathbf{y}) \cdot \mathbf{n}(\mathbf{y}) dS(\mathbf{y}), \end{aligned}$$

where \mathbf{n} is the outer unit normal to Ω_ε , and

$$\mathbf{n}(\mathbf{y}) = \frac{\mathbf{x} - \mathbf{y}}{|\mathbf{x} - \mathbf{y}|} \triangleq \frac{\mathbf{r}}{|\mathbf{r}|}.$$

Hence, on the one hand,

$$\begin{aligned} F_{\partial\Omega}(\mathbf{c}, \varepsilon) &\triangleq \int_{\overline{C_\varepsilon}} (\nabla\Phi_c - \mathbf{c} \cdot \Phi_c)(\mathbf{x} - \mathbf{y}) \cdot \mathbf{n}(\mathbf{y}) dS(\mathbf{y}) \\ &= \int_{\overline{C_\varepsilon}} \frac{1}{4\pi|\mathbf{r}|} e^{1/2(\mathbf{c} \cdot \mathbf{r} - |\mathbf{c}||\mathbf{r}|)} \left(-\frac{1}{|\mathbf{r}|} - \frac{\mathbf{c} \cdot \mathbf{r}}{2|\mathbf{r}|} - \frac{1}{2}|\mathbf{c}|\right) dS(\mathbf{y}) \\ &\leq \int_{\overline{C_\varepsilon}} \frac{1}{4\pi|\mathbf{r}|} e^{(-|\mathbf{c}||\mathbf{r}|)} \left(-\frac{1}{|\mathbf{r}|}\right) dS(\mathbf{y}) \\ &= \frac{1}{4\pi|\mathbf{r}|} e^{(-|\mathbf{c}||\mathbf{r}|)} \left(-\frac{1}{|\mathbf{r}|}\right) \int_{\overline{C_\varepsilon}} dS(\mathbf{y}) \\ &= \frac{1}{4\pi\varepsilon} e^{(-|\mathbf{c}|\varepsilon)} \left(-\frac{1}{\varepsilon}\right) \int_{\overline{C_\varepsilon}} dS(\mathbf{y}) \\ &= \frac{1}{4\pi\varepsilon} e^{(-|\mathbf{c}|\varepsilon)} \left(-\frac{1}{\varepsilon}\right) \cdot \left(\int_{\overline{C_\varepsilon}} dS(\mathbf{y}) + O(\varepsilon^3)\right) \quad (\text{by Lemma 2}) \\ &= -\frac{e^{(-|\mathbf{c}|\varepsilon)}}{2} + O(\varepsilon) \triangleq F_3(\mathbf{c}, \varepsilon), \end{aligned}$$

where the expansion and contraction process of the omitted techniques of inequalities is the same as the calculation of $F_1(\mathbf{c}, \varepsilon)$. On the other hand,

$$\begin{aligned} F_{\partial\Omega}(\mathbf{c}, \varepsilon) &\geq \frac{1}{4\pi|\mathbf{r}|} \left(-\frac{1}{|\mathbf{r}|} - |\mathbf{c}|\right) \int_{\overline{C_\varepsilon}} dS(\mathbf{y}) \\ &= \frac{1}{4\pi\varepsilon} \left(-\frac{1}{\varepsilon} - |\mathbf{c}|\right) \int_{\overline{C_\varepsilon}} dS(\mathbf{y}) \\ &= \frac{1}{4\pi\varepsilon} \left(-\frac{1}{\varepsilon} - |\mathbf{c}|\right) \cdot \left(\int_{\overline{C_\varepsilon}} dS(\mathbf{y}) + O(\varepsilon^3)\right) \quad (\text{by Lemma 2}) \\ &= -\frac{1}{2} - \frac{|\mathbf{c}|\varepsilon}{2} + O(\varepsilon) \triangleq F_4(\mathbf{c}, \varepsilon). \end{aligned}$$

Taking the limit as $\varepsilon \rightarrow 0^+$, we have

$$\lim_{\varepsilon \rightarrow 0^+} F_3(\mathbf{c}, \varepsilon) = -\frac{1}{2}, \quad \lim_{\varepsilon \rightarrow 0^+} F_4(\mathbf{c}, \varepsilon) = -\frac{1}{2}.$$

Therefore, it can be inferred from the squeeze theorem that

$$\lim_{\varepsilon \rightarrow 0^+} F_{\partial\Omega}(\mathbf{c}, \varepsilon) = -\frac{1}{2}.$$

In other words, $\forall \mathbf{c}, \forall \mathbf{x} \in \partial\Omega$,

$$\int_{\partial\Omega} K_c(\mathbf{x} - \mathbf{y}) \cdot \mathbf{n}(\mathbf{y}) dS(\mathbf{y}) = \frac{1}{2}. \quad \blacksquare$$